MRI compatible miniature motor system: Proof of Concept

René Haugsdal

A thesis submitted for the degree of Master in Physics: Measurement Technology and Instrumentation

November 2019

Department of Physics and Technology

Faculty of Mathematics and Natural Sciences

"All we have to decide is what to do with the time that is given us."

J.R.R. Tolkien

Abstract

The purpose of this project is to develop a proof of concept for a magnetic resonance imaging (MRI) compatible miniature motor control system. Possible applications for this include motion detection, motion control and robotic assisted intervention, all during an MRI scan.

Utilizing motorized actuation during an MRI scan introduces a host of challenges. Notwithstanding the magnetic environment, the severe and often times more complex issue is electromagnetic interference (EMI).

MRI relies on received radio frequency (RF) signals for generating images. RF receivers are highly susceptible to noise generated by external electrical equipment present in the MRI environment. Safety concerns arise due to the nature of the strong magnetic fields and the high frequency RF pulses present. Typically, these issues revolve around heating through resonance and antenna effects.

This thesis work consists of an introduction to basic MRI technology, evaluation of motor technology and testing of a chosen technological approach initially deemed MRI compatible. Defining, designing and testing of motor and material characteristics, including basic MRI environment functionality, are also included in the work.

It is shown that the motor is capable of driving an actuator during an active MRI scanning sequence, and that the ground work done in this project can serve as a basis for further development of an MRI compatible miniature motor.

Acknowledgements

This thesis is written in collaboration with Nordic NeuroLabs (NNL) and University of Bergen (UoB), Department of Physics and Technology, and was submitted for the M.Sc. degree in Physics: measurement technology and instrumentation.

I would like to thank my co-supervisors Olav Birkeland and Stian Sagevik at NNL, and supervisor Bjørn Tore Hjertaker at UoB. Olav Birkeland has been extraordinarily helpful, providing insight, technical assistance and invaluable advice throughout this entire project. Stian Sagevik has continuously helped in keeping me focused on the goals of this project, and was instrumental in giving me a starting point for the research on MRI safety and compatibility.

Moreover, Professor Hjertaker for constantly reminding me about the importance of the writing process and for always being willing to assist with funds, technical advice and for many valuable conversations in the office.

Thank you to Svein Reidar Rasmussen at NNL for providing assistance for and during MRI testing and for relying on me during equipment testing of NNL hardware, it was worthwhile and very valuable. Another thank you to Christopher Ulrich at NNL, for providing assistance with 3D printing, mechanical design challenges and sound advice.

I would also like to thank my grandfather Svein, for always answering questions and explaining physics to me when I was a child, I will always remember and cherish those times. Thank you for believing in me, dad. Thank you Cecilie, for showing me the door still existed.

My dear girlfriend Kristin, thank you for always being willing to listen and providing me the opportunity and challenge of explaining complex physics in simple ways.

This thesis would not have been possible without the structural, technical and motivational support from any one of you.

Contents

List of Figures

List of Tables

List of Abbreviations

AC	**A**lternating **C**urrent
CAD	**C**omputer **A**ided **D**esign
CC	**C**onstant **C**urrent
CV	**C**onstant **V**oltage
DAC	**D**igital **A**nalog **C**onverter
DC	**D**irect **C**urrent
DSV	**D**iameter **S**pherical **V**olume
EM	**E**lectro **M**agnetic
EMI	**E**lectro **M**agnetic **I**nterference
FID	**F**ree **I**nduction **D**ecay
FOV	**F**ield **o**f **V**iew
FSE	**F**ast **S**pin **E**cho
fMRI	**f**unctional **M**agnetic **R**esonance **I**maging
FWM	**F**ort **W**ayne **M**etals
GUI	**G**raphic **U**nit **I**nterface
HUS	**H**aukeland **U**niversity **H**ospital
IDE	**I**ntegrated **D**evelopment **E**nvironment
MCU	**M**icro **C**ontrol **U**nit
MEMS	**M**icro **E**lectro **M**echanical **S**ystems
MIU	**M**agnetic **I**nterface **U**nit
MOSFET	**M**etal **O**xide **S**emiconductor **F**ield **E**ffect **T**ransistor
MR	**M**agnetic **R**esonance
MRI	**M**agnetic **R**esonance **I**maging
NMR	**N**uclear **M**agnetic **R**esonance
NNL	**N**ordic **N**euro **L**abs
NTC	**N**egative **T**emperature **C**oefficient
OCP	**O**ver **C**urrent **P**rotection
OVP	**O**ver **V**oltage **P**rotection
PCM	**P**hase **C**hanging **M**aterial
PCB	**P**rinted **C**ircuit **B**oard
PSU	**P**ower **S**upply **U**nit
PZT	Lead **Z**irconate **T**itanite

RF	**R**adio **F**requency
SAR	**S**pecific **A**bsorption **R**ate
SMA	**S**hape **M**emory **A**lloy
TWSME	**T**wo **W**ay **S**hape **M**emory **E**ffect
USB	**U**niversal **S**erial **B**us
VSHD	**V**isual **S**ystem **H**igh **D**efinition
VCOM	**V**irtual **C**ommunication **P**ort

List of Symbols

ω	angular frequency
$\mathbf{s}$	arc length
μ_B	bohr magneton
$\mathbf{C}$	capacitance
q	charge
D	diameter
$\mathbf{E}$	electrical field
Ω	electrical resistance
ϵ	electromotive force
E	energy
F	Force
G	gain factor
g	gravitational constant
γ	gyromagnetic ratio
$\mathbf{L}$	inductance
K	Kelvin
ω_L	Larmor frequency
L	length
$\mathbf{B}$	magnetic field
Φ_B	magnetic flux
μ_m	magnetic moment
μ_0	magnetic permeability
χ	magnetic susceptibility
M	mass
r	radius
$\hbar$	reduced Planck constant
ρ	resistivity
s	spin
e	strain
τ	stress
A	surface area

T	Temperature
$\mathbf{T}$	Tesla
τ	torque
$\tilde{\mathbf{M}}$	total magnetization vector
$\vec{S}$	total spin angular momentum
V	Voltage
λ	wavelength

Chapter 1

Introduction

1.1 Motivation

The purpose of this master project is to develop a proof of concept for a miniature motor system for use in the adverse magnetic conditions posed inside an MRI scanner.

Currently, no commercial device for general motorized actuation in an MR environment is readily available. MR is a radiation safe medical imaging modality and represents a fair majority of the health hazard free imaging diagnostic tools available. Possible application examples include MRI aided robotic surgical actuation, positioning control systems during MRI and functional MRI (fMRI) examinations, tactile stimuli and braille devices.

There are two intertwined concerns for any external device introduced to an MRI environment; compatibility and safety. Is the device and the device materials MR safe, i.e., are they magnetically susceptible under all conditions posed in the scanner room or are there conditional limitations on how close it can be positioned to the MRI scanner. Two, if the device is MR safe, conditional or otherwise, what are the effects during scanner operation both by and to the device.

1.2 Background

The development of a MR compatible miniaturized motor control system has yet to be realized as a commercial product. However, several specialized solutions exist. Recent decades have seen a considerable growth in research and development with improved working approaches and new and unique implementations being explored.

Existing examples include, but are not limited to; prostate intervention [1], breast biopsy [2], neurosurgical intervention [3] and tumor thermotherapy [4]. Implementations of MRI compatible devices are motivated by the potential of the superior image guidance provided.

The majority of existing MRI compatible devices that require controlled actuation are piezoelectric [5], as opposed to traditional actuation technologies, e.g. electromagnetic, hydraulic or pneumatic. Part of the reason for this development is due to the obvious advantages in miniaturization. Miniaturization is the reason that piezoelectric motors have been extensively explored for use in MRI environments.

Another important reasons is the use of non ferromagnetic materials in piezoelectric motors. In addition, the piezoelectric motor efficiency has no size dependency, no maintenance, no lubrication, high speed and low power consumption whilst providing accurate positioning capabilities [6, 7]. These factors have placed piezoelectric motors at the forefront in MRI compatible robotics research.

However, the downside to piezoelectric designs is the requirement of large supply voltages (AC) to operate, which generates large amounts of electrical noise and inadvertently affects MRI image quality. RF shielding not withstanding, this is a complicated problem that currently does not have any universal solution. This is a main motivator as to why alternative approaches to piezoelectric based technology is explored for use in MRI environments.

1.3 Objective

The purpose of this project is to develop a miniature motor design that can serve as a basis for future integration with MRI compatible devices as an actuation controller. The project starts with an introduction to basic MRI technology, magnetism, evaluation of technologies available and a proposed solution for a miniature motor design.

The proposed miniature motor design is initially characterized. This means mapping of power requirements, stability, repeatability, controllability and MRI compatibility. The process also involves developing a method for the evaluation of the proposed design, through the development of a test bench and a measurement setup to facilitate the characterization process.

The measurement setup includes data acquisition, signal processing, circuit design and an embedded system to be made and configured. Designing and configuring the measurement setup as a whole requires applied knowledge of multiple measurement and modelling principles, all of which are detailed in appropriate sections. Lastly, the MRI compatibility testing is comprised using appropriate material and device testing performed at Haukeland University Hospital (HUS), at the available MRI facilities used by NNL for general testing purposes there.

This encompasses initial MR safety, visibility and compatibility, i.e, testing of magnetic susceptibility, artefact generation, visibility, RF heating and functionality. However, before this process can start, thorough research of the underlying physics of magnetism, MRI technology and other potential relevant principles will have to be performed.

Chapter 2

Theory

2.1 Nuclear magnetic resonance

MRI systems utilizes the nuclear magnetic resonance (NMR) phenomenon of protons in hydrogen atoms of unbound water molecules in the human body. The reason being the abundance of water content in the human body, $70 \pm 10\%$ [8]. The water distribution differs depending on the given tissue (organs, fat, muscle). The quantum mechanical properties of nuclear magnetic resonance in the unbound hydrogen atoms are the signal sources exploited in MRI technology.

All particles have fundamental quantities, such as mass (M) and charge (q). They also have an intrinsic quantum mechanical property known as spin (s), which has the SI units of [N m s]. This section only considers the spin angular momentum of a nucleus, and the direct relevance to the NMR phenomenon utilized in MRI.

Protons are spin-half particles, $s = \frac{1}{2}$. In the absence of an external magnetic field, protons have ground state spin degeneracy, $E = 2s + 1 = 2$. When protons are placed in a magnetic field they align to the magnetic field lines in one of two ways; parallel or anti-parallel, equating to lower and higher energy state respectively.

For a simplified two proton system consideration this phenomenon is known as a Zeeman split. The energy level difference between the parallel and anti-parallel spins are proportional to the magnetic field (**B**) and the Bohr magneton (μ_B). For in-depth discussion of spin, see [9] chapters 3 and 4.

For protons, the total spin angular momentum, equation 2.1, has z-component 2.2, see [10] chapter 43. The choice of a z-direction is essentially arbitrary. From an MRI conventional standpoint it becomes apparent as the static magnetic field direction is defined along the z-axis.

$$\vec{S} = \hbar\sqrt{s(s+1)} = \hbar\sqrt{\frac{1}{2}(\frac{1}{2}+1)} = \hbar\sqrt{\frac{3}{4}} \tag{2.1}$$

$$\vec{s_z} = \pm\frac{1}{2}\hbar \tag{2.2}$$

Simply put, the spin makes the proton act as a magnetic dipole when placed in an external magnetic field. Associated with this magnetic dipole is a spin magnetic moment (μ_m). The spin magnetic moment is defined in equation 2.3.

$$\vec{\mu_m} = g\frac{q}{2m}\vec{S} = \gamma\vec{S} \tag{2.3}$$

$g\frac{q}{2m} = \gamma$, where γ is the gyromagnetic ratio and $\vec{S}$ is the spin. The gyromagnetic ratio is defined as the particle or systems' ratio of magnetic moment to its angular moment. γ has units of $[\mathrm{rad/s/}\mathbf{T}]$. Combining 2.2 and 2.3 gives the following expression,

$$\vec{\mu_m} = \pm\frac{1}{2}\gamma\hbar \tag{2.4}$$

If a particle with a magnetic moment $\vec{\mu_m}$ is exposed to an external magnetic field $\vec{\mathbf{B}}$, it will as briefly explained above, align either parallel or anti-parallel to the applied field. In the simplified case of considering all moments aside from the spin magnetic moment, $\vec{\mu_m}$ represents the total magnetic moment of a proton. The sum of all magnetic moments in an arbitrary volume can then be summarily written as $\sum_{i=1}^{n} \mu_i = \vec{\mathbf{M}}$.

$\vec{\mathbf{M}}$ is the total magnetization vector. The interactions between $\vec{\mathbf{M}}$ and $\vec{\mathbf{B}}$ is neatly described in classical physics by the Bloch equation. A general expression of this is given in equation 2.5, for derivation and thorough discussion see [11], chapter 2.

$$\frac{d\vec{\mathbf{M}}}{dt} = \gamma(\vec{\mathbf{M}} \times \vec{\mathbf{B}}) \tag{2.5}$$

The first thing to note is that the vector product $\vec{\mathbf{M}} \times \vec{\mathbf{B}}$ is a vector perpendicular to both $\vec{\mathbf{M}}$ and $\vec{\mathbf{B}}$ and proportional to γ. It also has magnitude $|\vec{\mathbf{M}}||\vec{\mathbf{B}}|sin\alpha$, as defined by the general vector cross product. This tells us that $\frac{d\vec{\mathbf{M}}}{dt}$ moves in precessional motion, with angular frequency $\omega = \omega_L$. This is defined as the Larmor equation 2.6,

[11].

$$\omega_L = \gamma|\vec{\mathbf{B}}| \tag{2.6}$$

The Larmor frequency (ω_L) is proportional to the applied magnetic field. The Larmor frequency for protons is $42.6\,\mathrm{MHz}/\mathbf{T}$. Protons are the only considered signal source for MRI [11]. Generally speaking, the static magnetic field and the x-, y- and z- gradient magnetic fields manipulate the precessional motion and Larmor frequency of the selected cross sectional areas of a target body.

RF pulses are then employed to excite the spin system. The RF waves couple with the spin system by adding energy. This makes the spins flip away from the equilibrium positions along the z-axis. The described behavior is a purely quantum mechanical effect and is explained in detail in [9], chapter 3.

Due to the conservation of angular momentum, the spins decay back to their original equilibrium positions. During this process they radiate energy, which is detectable, and it induces low level currents in the RF receiver coils. This is known as the free induction decay (FID) signal. The signal, and derivations of it, are the measured quantity employed in MRI systems, and the foundation of NMR as an imaging modality [9, 11].

2.2 Magnetic fields in the MR environment

The magnetic fields in an MRI scanner are generated by electromagnets. The general principle of the magnetic field generated by the electromagnet is found in the relation between the electric current and the associated magnetic field generated by the current. This is expressed through Biot and Savart's law:

$$d\vec{\mathbf{B}} = \frac{\mu_0 I}{4\pi r^3}\vec{\mathbf{r}} \times d\vec{\boldsymbol{l}} \tag{2.7}$$

where I is the current, $d\vec{\boldsymbol{l}}$ is a vector with length dl, in the direction of the current in the conductor and $\vec{\mathbf{r}}$ is the vector between the current element $d\vec{\boldsymbol{l}}$ and the position where the magnetic field is measured. The complete magnetic field is then found by integrating elements $d\vec{\boldsymbol{l}}$ in equation 2.7, resulting in:

$$\vec{\mathbf{B}} = \frac{\mu_0}{4\pi}\int_C \frac{I d\vec{\boldsymbol{l}} \times \hat{\mathbf{r}}}{r^2} \tag{2.8}$$

As is evident, the magnetic field is a function of the overall geometry.

The definition of a modern MRI system is not constant. For the sake of convention, the increasingly common MRI scanner system have magnetic field strengths of $> 1.5\,\mathbf{T} - 7\,\mathbf{T}$. This is the magnetic field strength range referred to by modern MR systems. For a complete list of existing MRI systems, see [12]. All considerations, discussions and experiments described in this thesis are done with modern MR systems in mind.

Modern day MRI systems use superconductive magnets. A superconductive magnet simply means a magnet with a sustained temperature where the current flow does not experience any resistance. For this condition the magnet needs to be cooled below a maximum threshold temperature of $< 12\,\mathrm{K}$. To achieve this the magnetic coils are immersed in liquid helium, which holds a temperature of $4.2\,\mathrm{K}$ under ambient atmospheric conditions [11].

For illustrative purposes, a general picture detailing the different magnetic coils and the relative coil positions is shown in figure 2.1.

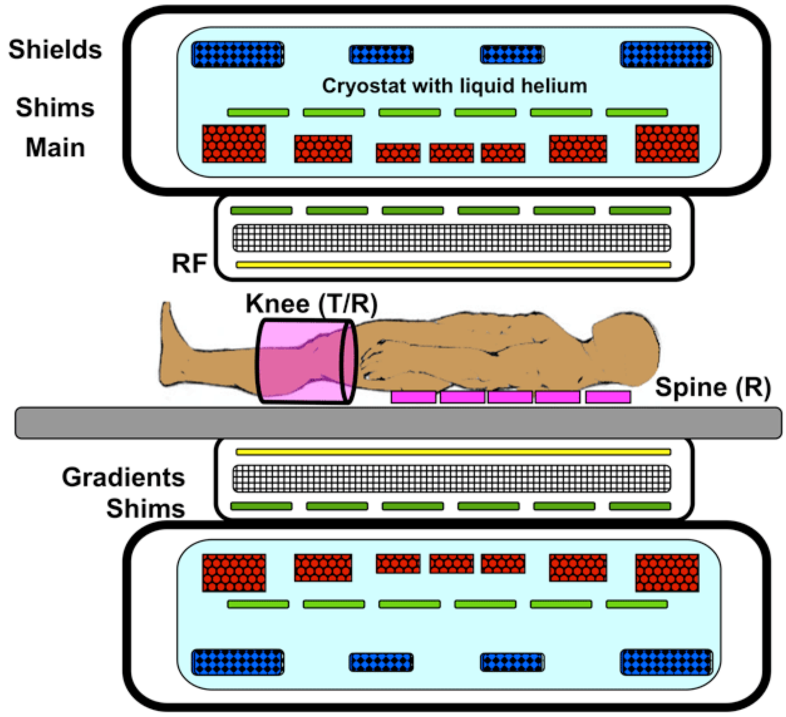

FIGURE 2.1: MR Coil system configuration illustration [13]

In the following sections, a short description on the different coils will be given, as well as a discussion of project relevant topics.

2.2.1 Static magnetic field

The static magnetic field $\mathbf{B}_0$ generated in the MRI system is always on, as a consequence of the superconductive magnet. As such, any objects within the MRI gantry are always exposed to the magnetic field $\mathbf{B}_0$. Even though $\mathbf{B}_0$ is called the static magnetic field, only a small part of the field can be considered homogeneous, classic coil current induced magnetic field is illustrated in figure 2.2, and further discussed in [11].

From simplified geometric considerations of a solenoid conductor it is plain to see from the field line configuration that the magnetic field gradient $\nabla\mathbf{B}_0$ is at maximum around outside of the solenoid, or for MRI scanners, the gantry. Furthermore, $\nabla\mathbf{B}_0 \approx 0$ inside the area of the tunnel referred to as the isocenter or imaging region [11], where the targeted body is placed for imaging figure 2.2.

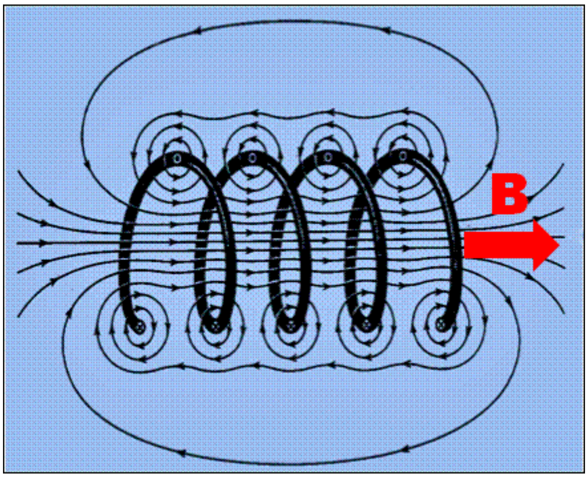

FIGURE 2.2: Solenoid magnetic field line representation [13]

Both the areas around the MRI gantry and the isocenter is of importance when considering potential effects of $\mathbf{B}_0$ on electric and mechanical systems. Magnetic flux Φ_B , change in magnetic flux $\Delta\Phi_B$ and potential heating effects are all examples of considerations which must be made when intending to use electromechanical systems in such an environment.

The remaining facets of $\mathbf{B}_0$ are relatively unimportant, as shielding around the room and the main magnet itself suppress the fringe field effects of $\mathbf{B}_0$. The general convention for magnetic field safety surrounding an MR system is defined as the $5\,\mathrm{G}$ line, or 5 Gauss line, equal to $0.5\,\mathrm{m}\mathbf{T}$ in magnitude [14, 15]. Outside of this line it is considered safe for ferromagnetic materials.

Magnetic field strengths vary from system to system, and it depends on the intended use (clinical, research etc), but generally the ranges are $1.5\,\mathbf{T} - 7.0\,\mathbf{T}$ in magnitude. As such, the 5 Gauss line is a relative distance calculated per system. In addition, it also depends on the design, geometry of the magnet, installation site and shielding of the fringe field [11].

2.2.2 Gradient magnetic field

The gradient magnetic field(s) are generated by three different magnetic coils, in the respective x, y and z-direction, mathematically represented by equation 2.9.

$$\mathbf{B}_{G,z} = \frac{d\mathbf{B}_z}{dx}x + \frac{d\mathbf{B}_z}{dy}y + \frac{d\mathbf{B}_z}{dz}z = G_x x + G_y y + G_z z = \vec{G} \cdot \vec{r} \tag{2.9}$$

The function of these coils is ideally to generate linear frequency variations in the Larmor precession of protons as a function of position. This is applied to spatial encoding of signal sources in relation to $\mathbf{B}_0$ and provides a way to segment signal sources. It is essential to the image processing in MRI systems.

The gradient coils can be constructed in a multitude of ways [16]. Since the concern is the basic principle, consider loops of wire coils inside the MRI gantry, conceptually shown in figure 2.3 for the z-gradient coil based on the reverse Helmholtz design. The reverse Helmholtz design is widely used due to the coil pair producing a uniform magnetic field gradient along the coil pair's axis [9].

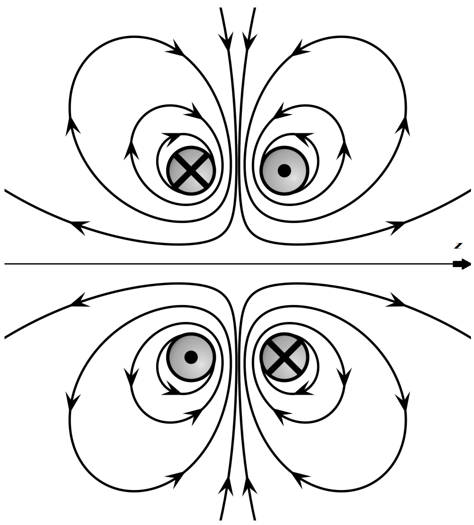

FIGURE 2.3: Helmholtz coil anti alignment configuration [17]

General convention for the directions of the gradient coils are the z-direction in the same direction as the static magnetic field $\mathbf{B}_0$, with the x- and y-direction both being perpendicular to the each other and to the z-direction, as represented in mathematical terms in equation 2.9. An illustration of gradient coil placements is provided in figure 2.4.

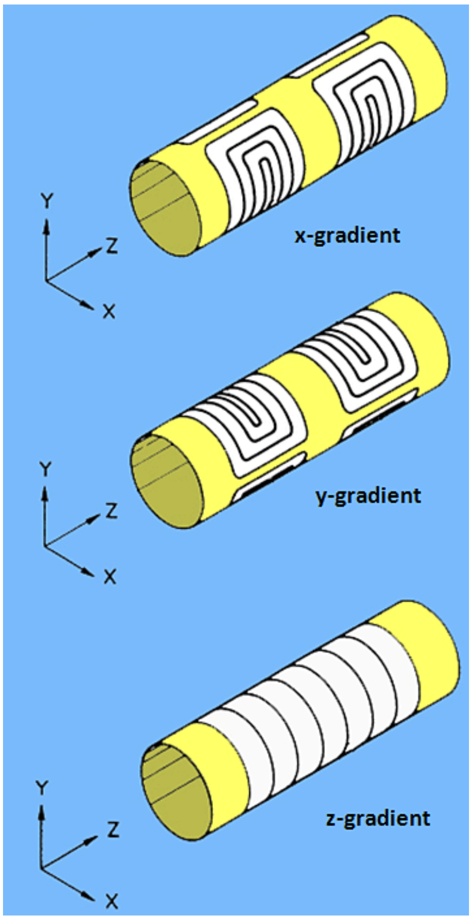

FIGURE 2.4: Gradient coil illustration [13]

The dimensions of G is $[\mathbf{T}/\mathrm{m}]$. According to Maxwell's equations, the field representations from 2.9 are in principle impossible. However, with low gradient fields they become a good approximation due to negligible influence of transverse components [11].

The gradient coils work by adding small linear gradient regions to localized places in the $\mathbf{B}_0$ field, which is also referred to as the scanner's imaging region. Gradient regions vary in magnitudes ranging from $40\,\mathrm{m}\mathbf{T}/\mathrm{m} - 80\,\mathrm{m}\mathbf{T}/\mathrm{m}$ from the Larmor frequency [14].

One important quality regarding gradient coils relevant for the discussion is the slew rate. Slew rate is defined as the change in a given quantity with respect to time. For our purposes this means change in magnetic field strength with respect to distance and time, with units of $[\mathbf{T}/\mathrm{m}/\mathrm{s}]$.

Qualitatively this describes how fast a gradient field can go from zero to maximum value and vise versa. Typical slew rates for modern MRI scanners are $200\,\mathbf{T}/\mathrm{m}/\mathrm{s}$

[14]. A higher slew rate also effectively means better imaging clarity, which is an important aspect for diagnostics. However, a higher slew rate also means a much more costly machine, so there is a cost benefit balance to it.

Furthermore, the gradient magnetic field orientation is easily reversible by changing the direction of current flow in the gradient coils using advanced class D (switching) amplifiers [18]. This, combined with the typical slew rates gives rapidly switching gradient fields of $< 1\,\mathbf{T}/\mathrm{m}/\mathrm{s}$. Large voltages ($\geq 2000\,\mathrm{V}$) and currents ($\geq 800\,\mathrm{A}$) are common in modern MRI scanners [19].

2.2.3 RF electromagnetic field

RF coils are responsible for transmitting and receiving RF signals from the object or person of scanning interest. This interaction is made possible by the coupling of the transmitted RF signal's transverse field and the nuclear magnetic spin moment of precessing hydrogens, which subsequently flip their spins out of the equilibrium positions along the z-axis. For in depth treatment of the transverse RF field coupling to nuclear magnetic spin, see chapters 3 and 9 of [9].

The signal generated in the RF coils are commonly referred to as RF pulses, due to the short duration ($\mu\mathrm{s} - \mathrm{ms}$). The magnetic fields the RF pulses generates are referred to as $\mathbf{B}_1$ fields, and are several magnitudes lower than $\mathbf{B}_0$, but have high frequency [14].

The same transmitting RF coils work as receivers as they measure the relaxation of the precessing hydrogens moving back to their respective equilibrium state in the z-direction imposed by the static and gradient fields. This induced response in the receiver coils is commonly referred to as a free induction decay or FID signal in MRI literature [9, 11].

Modern MRI scanners usually have the transmitter and receiver coils located innermost in the gantry in what is referred to as a body coil. This is apart from the fMRI examinations, where the transmitt and receiver coils can both be located in a separate head coil connected inside the gantry, much closer to the patients head, thus having better imaging capabilities.

2.3 MR safety and compatibility

2.3.1 Magnetic field shielding and shimming

Shielding of $\mathbf{B}_0$ serve to dampen fringe field effects, as no shielding of the main magnet would potentially cause the 5 Gauss line to extend beyond the confines of the room containing the MRI scanner, in all directions. Additionally, shielding causes the static field gradient to increase as a direct consequence of confining the greater magnitude to a smaller radii. This represents additional and unavoidable safety conditions and is therefore of major design concern.

Modern systems predominantly apply active shielding. Active shielding means having a set of secondary coils superimposed on the main coils of $\mathbf{B}_0$, as illustrated in figure 2.1 by the green blocks. The secondary shielding coils have current running in opposition to the main coils, as this generates the opposing magnetic field responsible for the shielding effect. This is preferred to passive shielding, as scanners with field strengths of $\geq 1.5\,\mathbf{T}$ would require iron cores weighting $\approx 20\,000\,\mathrm{kg}$ minimum, for necessary fringe field suppression. Iron cores also have varying magnetic fields due to temperature dependent magnetic susceptibility [11, 9].

The main magnetic field cannot be fully determined until the magnet has been physically placed at the installation site, due to effects from any potential external magnetic sources [11]. Only after final placement can the process of field mapping and calibration be performed. In order to determine the actual field configuration, the static magnetic field is thoroughly mapped using magnetometers and spherical computer models along with additional tools detailed in [20]. Spherical harmonics play a huge part in modelling the deviations and levels of homogeneity. The magnetic field distribution can be represented via the general Laplace equation 2.10.

$$\nabla^2\vec{\mathbf{B}} = \nabla^2(\vec{\mathbf{B}}_x + \vec{\mathbf{B}}_y + \vec{\mathbf{B}}_z) = 0 \tag{2.10}$$

For $\mathbf{B}_0$ homogeneity considerations applied in the z-direction, equation 2.10 then reduces to equation 2.11.

$$\nabla^2\vec{\mathbf{B}}_z = 0 \tag{2.11}$$

The general solution [21] to equation 2.11 is shown in equation 2.12.

$$\mathbf{B}_z(r,\theta,\phi) = \sum_{n=0}^{\infty}\sum_{m=0}^{n}[A_{nm}cos(m\phi) + B_{nm}sin(m\phi)]P_{nm}r^n cos(\theta) \tag{2.12}$$

Where A_{nm} and B_{nm} are series coefficients and P_{nm} are associated Legendre functions, for a full and complete discussion see [11, 22, 23]. In relation to the shielding and shimming discussion, a Taylor series expansion of equation 2.12 provides a clearer picture, detailed in equation 2.13.

$$\mathbf{B}_{actual} = \mathbf{B}_0 + 3\ (\text{linear terms}) + 5\ (2^{nd}\text{order terms}) + 7\ (3^{rd}\text{order terms}) + 9\ (4^{th}\text{order terms}) \ldots \tag{2.13}$$

The actual magnetic field is approximated with n > 1 terms representing increasing levels of complexity in disturbances to the homogeneity of the ideal field, $\mathbf{B}_0$. The ideal field representation being $\mathbf{B}_0$ [24]. Equation 2.13 is directly relevant to shimming, as shimming coils (active) and or iron elements (passive) are placed at appropriate locations in and around the gantry to optimize and characterise the final desired static field configuration.

The homogeneity of the system is quantified by; parts-per-million (ppm) of a given diameter spherical volume (DSV). Newer systems have reported value ranges of $\approx 1\,\text{ppm} - 1.5\,\text{ppm}$ and $DSV \approx 50\,\text{cm} - 60\,\text{cm}$, depending on scanner manufacturer [25, 26].

2.3.2 Static field effects

$\mathbf{B}_0$ represents the field of highest magnitude in a scanner environment, on average between 30 000-60 000 times stronger than earth's magnetic field strength at its surface. For external and internal devices brought into the MR environment this means having to consider potentially dangerous translational and rotational forces. Ferromagnetic materials are the most important safety concern with respects to $\mathbf{B}_0$ [14]. For ferromagnetic materials in magnetic saturation, that is, where $\mathbf{B}_0$ can no longer increase the internal magnetization as the material is in an ordered ferromagnetic state, we can quantify the translational and rotational effects, respectively.

$$\frac{F_{Trans}}{F_g} = C\mathbf{B}_s|\nabla\mathbf{B}_0|, \quad C = \frac{1}{\mu_0 g\rho} \tag{2.14}$$

$\mathbf{B}_s$ is the maximum flux density of the material, $|\nabla \mathbf{B}_0|$ is the magnitude of the static magnetic field gradient at a given point, μ_0 is magnetic permeability of free space, g is the gravitational acceleration constant and ρ is the material density. Similarly for rotational forces, the torque on a dipole μ_m in a magnetic field **B** is the vector cross product of the two quantities.

$$\tau = \mu_m \times \mathbf{B} \tag{2.15}$$

An important distinction between the translational (2.14) and rotational (2.15) forces is that translational force maximum effect occurs at the point where $\nabla \mathbf{B}_0$ is at a maximum, and zero at isocenter where $\nabla \mathbf{B}_0 = 0$. Conversely, the torque effect is at a maximum at $\nabla \mathbf{B}_0 = 0$. Value examples and in depth discussion provided in [14].

2.3.3 Gradient field effects

Gradient coils are used for spatial encoding in MRI, with units of [T/m], and field strengths ranging from $40\,\mathrm{m}\mathbf{T}/\mathrm{m} - 80\,\mathrm{m}\mathbf{T}/\mathrm{m}$ or more, as previously stated. If one assumes a general field of view (FOV) value of $40\,\mathrm{cm}$ with a gradient strength of $40\,\mathrm{m}\mathbf{T}/\mathrm{m}$, this equals a field strength of $10\,\mathrm{m}\mathbf{T}$ at the edge of a gradient field. Compared to the static magnetic field, the gradient field is several times lower in magnitude. Needless to say, other safety concerns revolve around the gradient field.

Safety concerns regarding the gradient field is the nature of the rapid switching of the field. The rapid switching can cause induced eddy currents in patients, implants or external devices placed in the MRI gantry during a scan. The induced eddy currents are a result of Faraday's law of induction shown below for completeness in equation 2.16. A consequence of this is a change in magnetic flux through a closed loop conductor causes loops of opposing currents to flow in the conductor [10].

$$\varepsilon = -\frac{d\Phi_B}{dt} \tag{2.16}$$

The opposing current loops generate heat due to ohmic resistance in a conducting material. However, this does not constitute a primary safety concern for gradient fields, as opposed to RF pulses. As mentioned in Section 2.3.2 additional eddy current effects include possible device and or material vibration due to the rapid switching nature of the gradient fields, leading to added acoustic noise and patient discomfort from tactile stimulus [14].

For humans, the prevalent safety concern regarding gradient fields are peripheral nerve stimulation and the extreme acoustic noise levels ($> 130\,\mathrm{dB}$) generated by the gradient coils due to high Lorentz forces experienced under high frequency current switching. For a complete followup on human, rather than external equipment safety considerations, the reader is encouraged to see [14, 15, 27, 28] for in depth discussion regarding specific absorption rates (SAR) and human implant safety considerations.

2.3.4 RF field effects

Radio frequency pulses represent the primary safety concern in relation to both patients, internal and external equipment in MR environments. The safety concerns are extensive, but can be roughly summarized as electromagnetic induction and/or antenna effects [14, 27, 29, 30, 31]. As stated above, the RF field has $\mu\mathbf{T}$ magnitudes making it lower than both static, gradient fields and the earth's magnetic field. It might then seem odd for RF to represent a major safety concern. Contrary to both the static and gradient magnetic field, the RF field consist of both a magnetic and electric field, colloquially referred to as $\mathbf{B}_1$ and $\mathbf{E}_1$ fields, respectively.

Additionally, the RF field has a frequency proportional to the system's Larmor frequency ($\omega_L = 42.6\,\mathrm{MHz}/\mathbf{T}$). The high frequency RF is what constitutes the risk factor. The frequency dependence of the RF field effectively means that the RF is dependent on the static magnetic field of the MRI system e.g. the RF field frequency is higher for a $3\,\mathbf{T}$ MRI than a $1.5\,\mathbf{T}$ MRI and so on.

Starting with electromagnetic induction, there are three principal conditions that causes heating to occur; eddy currents, induction loops and resonating RF waves along the conductors. The mechanism by which eddy currents occur are explained in section 2.3.3. For induction loops the focus is on conductive leads and/or guide wires. Conductive wires wound in loops are subject to induction via Faraday's law 2.16. This means more circulating currents flow and subsequent power dissipation of the immediately surrounding media.

Examples and tests have been performed with plastic boxes for an electric device and clothing or skin exposed to direct contact with a guide wire. This can cause failure in electric equipment, even burning of circuits and on patients' skin [14, 27]. For all electrical equipment introduced in MRI environments another concern is avoidance of resonance effects in circuitry and transmission cables providing power to external devices. Resonance effects represent the highest potential danger in form of rapid heating, dielectric breakdown (sparking) and even potential fire outbreaks [5, 14, 27, 30, 31, 32].

Simply put, resonance effects occur in an electric circuit when the voltage oscillates at a frequency which corresponds to the inductance (**L**) and capacitive (**C**) impedances are of equal magnitude and form a phase angle of 180° relative to each other, occurring at $\omega = \frac{1}{\sqrt{\mathbf{LC}}}$ [27].

Rapid heating is a resonance effect which is often observed at interfaces of media with different conductive properties. Essentially, this is described using a two layer interface model, where each layer has different impedance characteristics. Common examples of scenarios where this is likely to be an issue are transmission, coaxial connectors and guide wire insertion points, e.g. needle puncture. Moreover, rapid heating can also be caused by antenna effects from open ended conductors and guide wires. A guide wire exposed to an RF field will excite and store energy as a dipole antenna, see half wave dipole antenna models [29]. The electric $\mathbf{E}_1$ component of the RF field couples with the wire and causes standing waves to propagate along the wire with the same wavelength as that of the RF field.

The resonance phenomenon is dependant on multiple conditions. Primarily, it is critical that wire lengths of half a wavelength of the RF field are avoided, as this is the length at which a dipole antenna exhibits resonance at the wire ends. Since the wire ends are the sources of the gathered energy from the standing wave reflections, they exhibit spot heating at the ends and in the close vicinity [14, 27].

Safety testing protocols for rapid heating effects include placing lengths of the conductive wire at different locations in the MRI while running high RF demanding imaging sequences to determine the effects. The tests are usually performed a multitude of times with incrementally shorter and or longer wires for determining the optimal and worst case conditions. As previously stated, the resonance lengths are half wavelength dependent. A not so obvious effect of this is that if a wire or a conductor is placed such that it on any length point comes in contact with a different material, it will alter the effective resonance length of the material [14, 27, 31]. Generally speaking, the resonance length is shortened, due to the fact that most common contact materials, e.g. fabric, skin or plastic, have much higher impedance characteristics than conductors.

Lastly, it is worth mentioning that for patients, the appropriate quantity for the heating discussion is called specific absorption rate (SAR) and has units [W/Kg]. SAR relates the deposited energy in a medium to the rate of energy dissipation. It is a quantity not measurable but approximated through years of experiments, modelling and extensive testing [14].

2.3.5 MR compatibility

MRI compatibility encompasses a large set of topics, the ones relevant to this project will be detailed here. It starts with the basic material property that determines initial MRI compatibility, magnetic susceptibility. The quantity by which we can measure how much a given material is affected, or magnetized, by exposure to a magnetic field is defined as magnetic susceptibility, denoted as χ. For formal definitions and description of the various susceptibility models, see [9] chapters 3, 4 and [33] chapters II though IV. Simply put, it allows us to categorize a material according to whether χ is large and positive, χ is small and positive or χ is negative. This is respectively referred to as ferromagnetic, paramagnetic and diamagnetic materials.

Ferromagnetic materials is usually thought of as iron, nickel and cobalt, with iron being the most abundant material. Objects of ferromagnetic nature can be treated as projectiles if the magnetic forces acting on the object is greater than the gravitational forces. As such, the parameters of primary importance include the objects weight (kg), the susceptibility (χ) and the magnetic field magnitude $\mathbf{B}_0$, $|\mathbf{B}_0|$. Ferromagnetic materials are not considered MRI compatible. However, some metal composites can and do include ferromagnetic materials, yet are not magnetized by proximity to the $\mathbf{B}_0$ field, such as Nitinol, a material comprised of nickel and titanium [34, 35].

Relevant to this project's discussion on MRI compatibility are materials of low/negative magnetic susceptibility, or simply put, materials not affected by the static magnetic field. For such materials, or devices thereof made, tests are required in order to determine whether it is MRI compatible or incompatible. One of the tests performed is called a material visibility test. Simply put, a visibility test is a test where the material is placed on or near a known MRI phantom. An example of such an MRI phantom is a hollow plastic ball filled with liquid designed to mimic human tissue responses. This is to have clearly defined bounds within which the expected image is known, as it then becomes easy to verify if additional objects attached to the phantom are visible.

However, a visibility test serves an additional purpose. That is to look for potential artefact generation and/or signal loss. Artefact generation is a broad topic and includes a multitude of effects not directly relevant for this project, as such, for an in-depth description see [11, 36]. The artefacts of primary interest in this project are related to disturbances to the homogeneity of the static magnetic field $\mathbf{B}_0$ and the gradient magnetic field, and the potential for RF interference(s).

Disturbances to the homogeneity of the $\mathbf{B}_0$ field can cause images generated appear to have black spots with nothing on them, this is due to signal loss. These disturbances can be caused by multiple scenarios, the ones most relevant to the project are detailed here. Number one, any ferromagnetic material presence will inadvertently cause these kinds of artefacts, that concern should however be secondary considering the potential missile effects. Number two, if a conducting element such as a copper wire is placed in a coiled configuration on an imaging phantom, it will generate an opposing magnetic field due Faraday's law of induction detailed in Section 2.3.4. Number three, a conductor with a running current generates a rotating magnetic field locally around the conductor, as explained initially in Section 2.2, and from equations 2.7 and 2.8.

The scenarios briefly mentioned above cause local disturbances in the magnetic field homogeneity surrounding the material and/or conductor, thereby changing the RF energy required to excite the local free hydrogens, causing it to appear black, as there is no detectable energy of the proper radio frequency leading to the signal loss appearing as black spots on the image(s). These field homogeneity artefacts are usually not a severe problem for conductors powering external equipment, as they are typically located relatively far away from the imaging region of potential patients. Figure 2.5 below illustrates the homogeneity artefact.

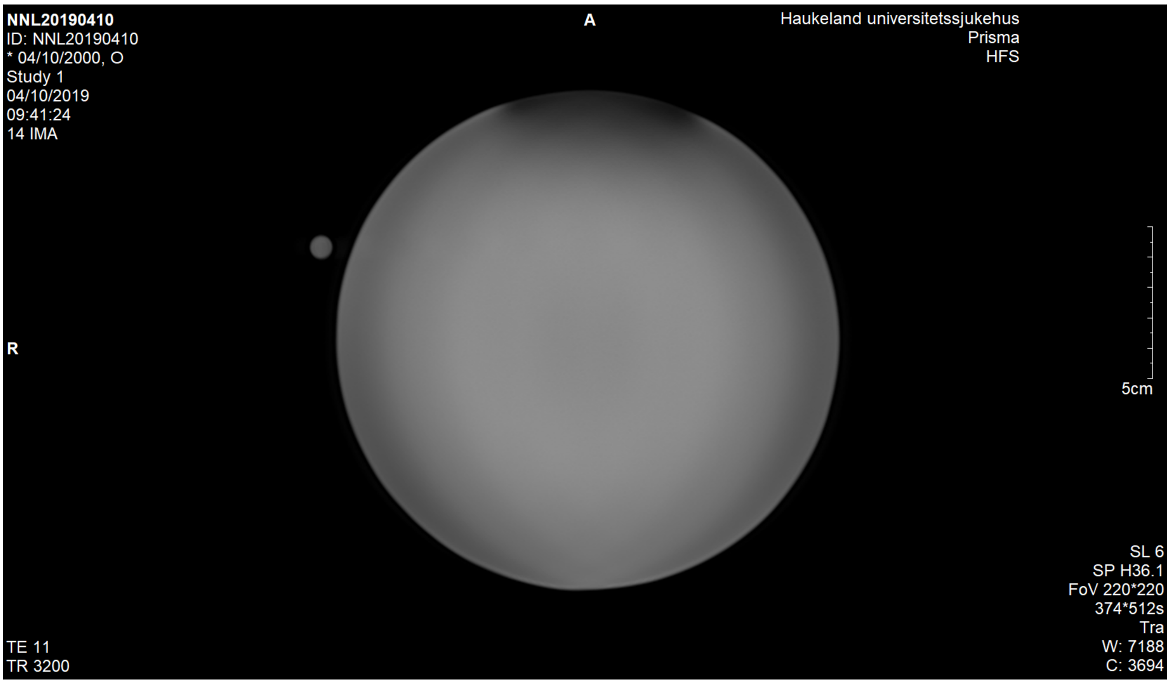

FIGURE 2.5: MR compatibility: Homogeneity artefact

This image is a slice selection of a spherical phantom with a coiled metal wire taped to it. The top of the image appears with a smeared black onto the phantom whereas the rest of it has a clearly defined boundary. The slight spot to the left of the image is of no concern to this discussion. For a broader discussion on these effects and surround phenomenons see [33] chapters V through VIII.

The above mentioned homogeneity effects are contrary to RF artefacts or RF noise. RF waves propagate omnidirectionally and the RF receiver coils located in the MRI scanner are capable of receiving RF energy from sources located far beyond the imaging region, even the 5 Gauss line. Additionally, RF noise is specific to the MRI scanner, given the Larmor frequency, equation 2.6, is magnetic field dependant the RF coils have associated frequency bands for RF detection. Generally speaking however, RF noise or interference comes in one and/or two forms; broadband noise near the Larmor frequency or harmonic frequency noise. Figure 2.6 below illustrates a phantom with a nearby RF source off and on, respectively.

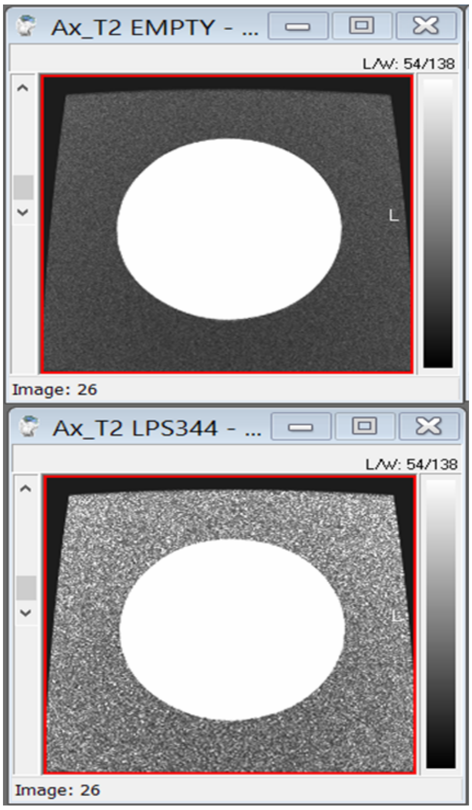

FIGURE 2.6: MR compatibility: RF background noise [37]

The broadband noise appears as a contrast diminishing grainy overlay on the entire image, and is easily seen when comparing the background of the top image to the background of the lower image. Background noise causes a through decrease in the signal-to-noise ratio (SNR). This effect is highly undesirable for diagnostic purposes, as a high contrast level is paramount to the identification of any potential condition(s).

Figure 2.7 below illustrates the harmonic effect on MRI images.

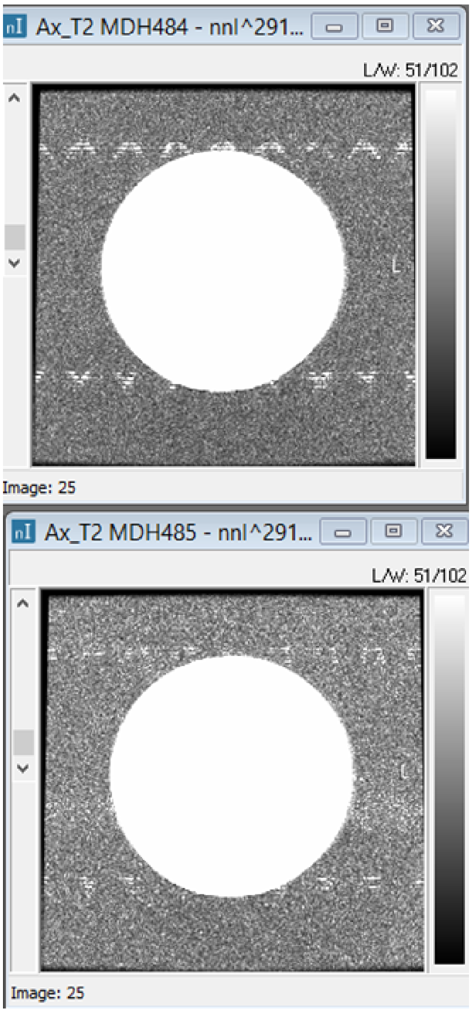

FIGURE 2.7: MR compatibility: RF harmonic noise [37]

For the harmonic frequency noise, the artefact(s) are clearly defined lines, to different degrees, on the image. This is due to the fact that the image processing is frequency dependant, since harmonics carry added energies to specific frequencies. Lastly, looking at MRI images are not the only means by which RF noise is detectable. Since contrast and brightness settings play a huge part in the visibility of these artefacts, more advanced tools are available. A standard tool used for RF noise detection is a spectrum/bandwidth analyser. Figure 2.8 shows the result graph of a Siemens built-in spectrum analyser with the MRI system.

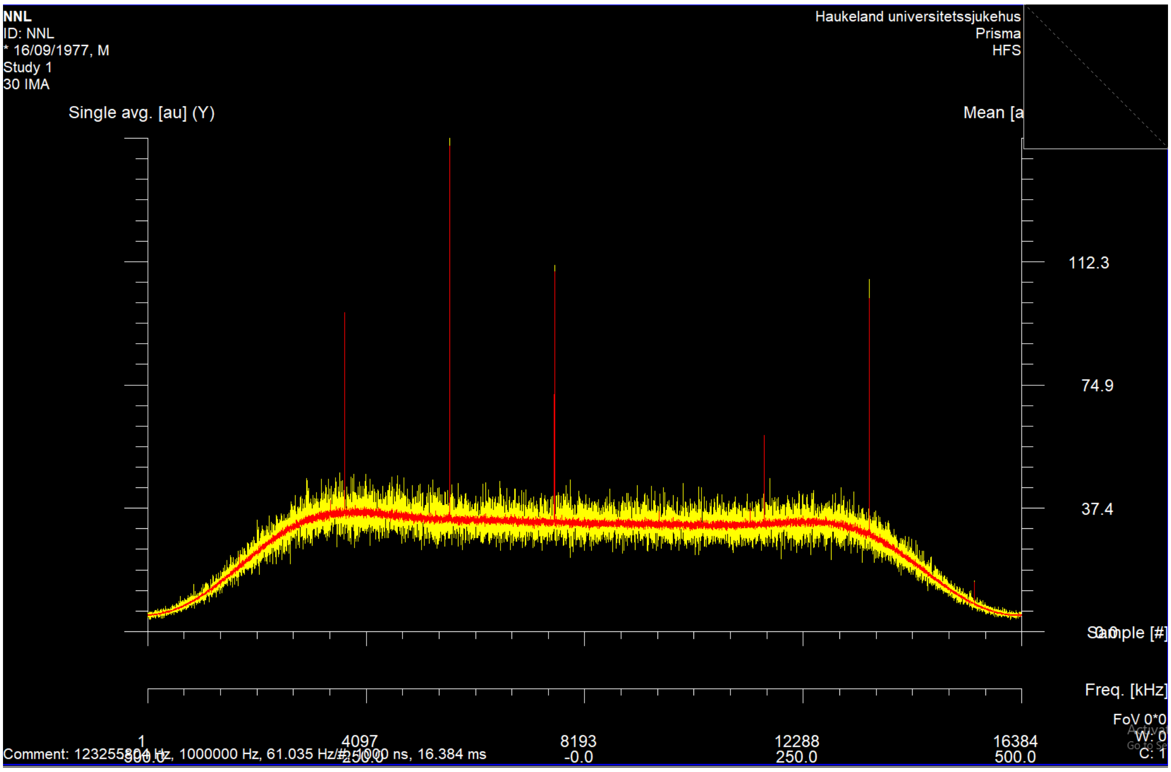

FIGURE 2.8: MR compatibility: RF harmonic noise [37]

The main point of figure 2.8 is to illustrate RF signal energies received by the RF coils in an MRI scanner. The graph shows the MRI system's RF bandwidth frequency on the x-axis, with the y-axes detailing both the mean and single average RF values. For interpretation, the thick red line with the fluctuating yellow are average and single average RF from the MRI system as a baseline for the RF energy spectrum. The 5 distinct red peaks are harmonic frequencies from a nearby located power supply.

These lines equate to the streaks observed in figure 2.7, with the higher peaks subsequently appearing as brighter in intensity in an MRI image. For more in-depth discussion related to image processing and frequency dependence, see [11] page 58-82.

2.4 Motor technology considerations

It is evident from the discussion presented above, that MRI compatibility is a complex topic and spans all aspects of motor system design. From requirements such as materials, components, power, frequency, size, and safety, the system design choice is limited from the very start. The exclusion of ferromagnetic materials and electromagnetic systems for use in an MRI environment is clear, due to safety concerns already addressed.

In addition to the safety concerns there is also the issue of compatibility. A multitude of potential negative effects are posed on the MRI scanner and the equipment when it is placed in the scanner room. Without extensive and proper shielding the list of effects are long, but some of the leading compatibility issues are artifact generation, image quality degradation, decreased homogeneity of the static magnetic field and a host of RF related issues. Hence, electromagnetic based systems are in general not considered MRI compatible [32, 38].

Conventional MRI gantry scanners of $\leq 3.0\,\mathbf{T}$ have bore diameters of $60\,\mathrm{cm}$ [39, 40], this means size restrictions for any external system or device brought into the MRI gantry along with a patient. Therefore, much of the recent research into MRI compatible motor control systems is based on Micro electromechanical systems (MEMS) [41]. However, MEMS design approaches often require sophisticated fabrication methods and funding, and the pursuit of a MEMS approach is considered well beyond the scope of this project. Larger scale specific solutions exist, e.g. prostate biopsy [42] and transmission guided intervention [43], and continued research in different directions than miniaturization.

It is necessary to point out that no attempt is given to provide a full list of available and possible approaches to MRI compatible miniature designs, such a list is beyond the scope and purpose of this project. However, detailed below are some approaches that were considered in light of this project.

2.4.1 Piezoelectric

Piezoelectric motors are by far the most represented method of actuation in MR compatible robotics, see [44, 45, 46, 47]. The main reason is that the piezoelectric effect is present in many magnetically inert and cheap materials, meaning cheap production and secured compatibility. Piezoelectric motor efficiency is insensitive with respect to size, as such, are inherently superior to pneumatic, hydraulic and electromagnetic designs. Due to the broad range of materials possessing piezoelectric properties, design specifications can be tailored to specific needs, [41] page 156.

It is well known that piezoelectric motor actuation has sub micron resolution capabilities. Actuator mechanisms come in large numbers of different designs, see an overview of piezoelectric motor history in [48], and can also be categorized according to the specific drive mechanism used e.g. resonance drive, inertia drive and piezo-walk drive.

Resonance drive motors work by causing displacement in the piezoelectric material by applying an AC signal at or close to the material's resonance frequency. This leads to amplified vibrations in the material. Rather than being proportional to the applied AC voltage amplitude, the vibrations are proportional to the signal(s) drive frequency [6].

Inertia drives consists of essentially three elements; a piezoelectric element, a counterweight and the body subject to displacement. The piezoelectric element is connected between the counterweight and the body. The counterweight is suspended from the surface and as such, it is not subject to friction forces unlike the body. A sawtooth signal is required to produce a displacement of the body [48].

The piezo-walk drive utilize the piezoelectric effect in materials to alter both lateral and shear strains in the material. This gives rise to mechanical motion such as elongation and bending of the material, comparable to the motion of a bimetal cantelever. Several piezo elements are connected to individually controlled voltages, in coordination they produce a walking like motion [48].

Piezoelectric elements are already well represented in miniaturized machinery. The precision, fast response times and self locks with no applied voltage all carry advantages over mechanical actuators when miniaturization is required. However, there are challenges to using a piezoelectric motor, which include high supply voltages, frequency and possible vibrations. For this project, a piezoelectric solution was considered but not pursued for several reasons.

The development of piezoelectric based technology requires in depth knowledge of both material and acoustic physics, it was felt that the entry level of expertise for this kind of a solution is beyond the scope of the participants of the project. Additionally, several commercial all purpose miniature piezoelectric solutions exist, making the MRI compatibility more a retrofitting project of potential incompatible elements in a bought product.

This was considered to be against the purpose of the project, as retrofitting of a bought product hardly classifies as development. Neither is it a good choice when considering the spirit of academic interest to pursue such a task. Last but not least, piezoelectric motors were in all considered too expensive given available funds.

2.4.2 Pneumatic actuator system

Pneumatic motors are gas based, and delivers motion in the form of compressed gas cylinders with pressure valves for controlling the delivered stroke. They can be made MRI compatible, but have inherent properties which makes them unsuited for precision actuation.

Pneumatic systems are highly nonlinear due to flow characteristics of servo valves and gas compressibility, as well as the actuator itself being nonlinear [49]. Friction, temperature and shape are all time varying quantities for a pneumatic system. Lastly, performances are further limited by o-ring performance and lifetime [39].

However, implementations using long transmission cables for actuation control have been considered [50]. As such, the use of transmission cables is one possible implementation of pneumatic actuation. Even EM coupled actuation can be considered, as it allows for the main motor system placement to be outside the scanner environment, this is desirable as it broadens the range of motor technologies available.

Various limitations include limited bandwidth and response delays depending on transmission cable stiffness and length, respectively. Furthermore, precision position control is made more difficult due to compression of the transmission cable medium. As such, position control may require additional elements, see [38] section IV for extended pneumatic discussion.

As the goal is the prototype development of a miniature motor integrateable with other systems, based on discussion and source research material, a pneumatic design will not be further pursued.

2.4.3 Hydraulic actuator system

Hydraulic systems are much like their pneumatic counterparts, other than the fact that a liquid medium instead of a gas is used to drive the displacement stroke. Hydraulic actuators can be made MRI compatible [51]. Compared to pneumatic actuators advantages include higher cable stiffness and durability.

However, like a pneumatic based system, a hydraulic system is also highly nonlinear. Mainly due to parameters such as uncertainties in pressure, friction, slippage, and orifice openings [38, 39]. Slippage in hydraulic systems is to the extent of our knowledge unavoidable at one level or another.

When taking this into account, along with transmission cable design for motor placements outside the scanner room, which in turn means longer response times and increased difficulty in accurate position control and leakage possibilities. It is concluded that a hydraulic based design implementation poses more challenges than benefits and is not considered a viable option for this project.

Worth noting however, is that a pneumatic solution would be preferable to a hydraulic, due to leakage not posing any safety concerns in a pneumatic system.

2.4.4 Thermal based actuator system

Most of the thermal based approaches rely on some form of volumetric expansion for actuation. General examples of this include state change (solid and fluid expansion) actuators and or some combinations of these. The main advantage to these approaches is high energy density, meaning they have high force and displacement outputs [41]. Due to the extremely large number of possibilities of thermal based actuators, we will only present two distinct approaches that have seen previous miniature designs. As such, these approaches do by no means encompass all possibilities available thermal based solutions.

Similarly, as ohmic heating will be the sole facilitator by which actuation is generated, other means of thermal actuation principles will not be discussed further. For a broader overview on different phase changing material (PCM) actuators and in depth discussion, see [52]. We start with the volumetric expansion from the solid to liquid phase change in materials. To this actuation principle several media could purposefully be used, provided they have a large thermal expansion coefficient as it is desirable for a miniaturized design.

One potential material that can be used is paraffin wax. Initially considered due to its high biocompatibility, thermal expansion property and low material cost [52]. The benefits to using paraffin wax as a miniature actuator includes significantly less complex modelling and ease of controlling delivered heating. Overall, it is a fair assumption that a miniaturization of this is of benefit to the overall response time , which is a good thing considering the general poor response times for thermoelectric systems. The phase change temperatures can be modified from ranges of $-50\,°\mathrm{C} - 100\,°\mathrm{C}$ according to desired specifications, depending on the number of carbon atoms in molecular chain of the wax [53].

However, volumetric expansion does not vary linearly with temperature, this together with an inherently large heat capacity makes it extremely problematic in terms of precise position control. Both the temperature distribution and heat capacity has a negative impact on any feedback system. The adjustments for precision movement is in the best circumstance a challenging prospect both in modelling and in application. In regards to MRI compatibility of paraffin wax only preliminary tests have been conducted [54]. Paraffin wax is not transparent on MRI images thus causing signal blockage by appearing visible. Hence, any use of a paraffin wax based actuator would have to be placed outside the imaging region, although further tests would be required for confirmation.

As it stands, wax actuation as a principle will not be pursued further, but constitutes a worthy mention due to the inherent simplicity in the approach, the low cost and the simplicity of its potential function.

Next, and last in our considerations is shape memory alloys (SMA). SMAs are materials that undergo a solid solid phase change. The phase change is triggered by the application of stress or heat. This is a diffusionless transformation, meaning small homogeneous movement of atoms relative to the crystal lattice results in an overall change in the crystal lattice [52].

The transformations of SMAs are referred to as martensitic transformation when cooled to a given low temperature and austenite transformation when heated to a given high temperature. In order to achieve a transformation effect the alloy requires conditioning. There are two different methods for achieving martensitic and austenite transformations respectively; shape memory training and stress induced martensite training [52].

Early research on SMAs established guidelines in regards to miniature application advantages and limitations. SMA actuators are silent running, require low driving voltages, are relatively easy to production and have no gears or lubrication requirements. No movable parts reduce the spread of dust particles, which is an important point with regards to potential sensitive optics and electronics and in medical applications [55].

However, SMAs suffer from inherently low response time. This is mainly due to limited passive cooling effects for the restoration of the martensite phase. Interestingly, a miniature design is beneficial as a small diameter SMA wire have increased heat dissipation due to the larger surface to volume ratios. Lastly, repetition and material fatigue limit the actuator strain if long life cycles are a requirement [52].

The shape memory effect is temperature induced, as such, a natural choice for feedback parameter is the material temperature. However, research has shown that for SMA based controlled actuation temperature is not a preferred parameter for feedback control. SMA materials exhibit large temperature hysteresis in regards to austenite and martensite start and finish phase transformation temperatures.

Luckily, SMA research also shows there are a multitude of phase dependant internal variables more suitable for feedback control, such as resistance [55, 56, 57]. SMA electrical resistance is not a static value. Rather, it is phase dependent [52, 55, 57, 58], and thereby connected to the strain of the material.

Recent research [59, 60] show that the linear relationship between resistance and SMA phase is more complex in commercial SMA materials than previously thought. All though resistance and strain have a documented and proven some degree of non-linearity, accurate and stable precision control with resistance feedback have been achieved. Albeit with complex use of neural networks or with closed loop PID control setups, e.g. [61].

The negative side to the use of SMA based actuators aside from the engineering challenge it poses, is that the deformation is heat induced and that the wire requires a constant current in order to hold a position. For position control of shutters, lenses and other high precision system this could potentially be a severe drain on battery power or overall power requirements. Nevertheless, SMA materials represent an exciting research prospect due to several characteristics of the material. A common SMA material known as Nitinol is, despite being a composite of nickel and titanium, compatible with MRI environments [34, 35].

Depending on design specifications, Nitinol can be heated with direct current (DC). This is preferred to alternating current (AC) as it effectively minimizes the potential effects caused to and by the RF coils. This opens for the potential of driving an actuation while the MRI system is in operation. Traditionally this has been difficult to achieve within reasonable margins of compromise due to image quality and safety concerns.

The problems with running a motor during an active MRI scan are several. For an SMA based system the initial concern is due to the way actuation is achieved. The effect of induced currents in the SMA wire and the leads connected to the wire can be a source of current fluctuations causing positioning instability. This is why a crucial component of the system design would revolve around the control system for the wire actuation.

Another aspect to consider is visibility, artefact generation and signal blockage. These effects are by default slightly mitigated by the fact that any proposed system would be shielded and confined as far away from the imaging region as possible. However, given the constant current required to maintain a given position, it is a concern and would have to be tested.

After consideration, and in the interest of further research prospects, it has been decided that SMAs are the preferred approach for further interest in this project. The motivators for this pursuit are several. First, it is already established from previous research that several types of SMAs are MRI compatible. Secondly, acquiring SMA samples for the project proved easy and convenient. A US based company named Fort Wayne Metals (FWM) [62], generously offered to provide SMA samples free of charge.

Also an important factor of consideration was simplicity. The method of SMA actuation is inherently simplistic, i.e. ohmic heating. This means with relative ease additional layers can be added to a skeleton experimental setup. Moreover, SMA actuation requires little or no additional expensive instrumentation for initial testing purposes, aside from the material itself which in this case was freely provided. Lastly, it is a material with fascinating and interesting properties. Coupled with a challenging engineering task makes it all the more appealing to explore further.

Chapter 3

Experiments

3.1 Preparation

The first thing necessary for setting up an experiment of this nature is to identify controllable and uncontrollable variables by the evaluation of potential setups. Once that has been established, a breakdown of the entire experiment into smaller steps can commence.

In light of the relatively young age of SMA actuator research, and the technical expertise level of the project candidate, it was necessary to start at the very basic level and build from there. This narrowed the prospective type of test setup considerably.

The most straight forward approach was to monitor both the temperature and the displacement directly. Since this proves an easy way of acquiring relevant measurements for SMA characteristic mapping without having to consider advanced models presented in many scientific articles [57, 59, 61]. It also provides a strong starting point for initial and further data acquisition. A block diagram of the system described in this section is provided in figure 3.1.

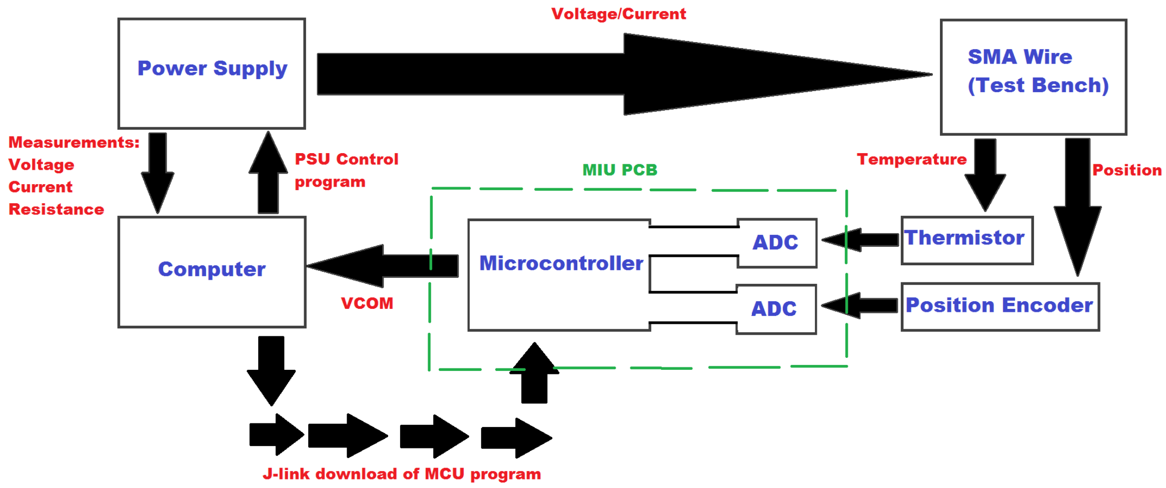

FIGURE 3.1: Block diagram of experiment

3.1.1 Equipment

The equipment used in every experiment is listed in table 3.1, not withstanding equipment used in specific circumstances, which will be detailed in their respective sections.

TABLE 3.1: Equipment list of experiments

#	Producer: Type	Description
1	K and H: Model RH-74	Bread Board
2	Electro-Automatik: EA-PS 2042-06B	Power Supply (Digital)
3	Toellner: Toe 8735	Power Supply (Analog)
4	Arm Cortex - M4F Kinetis K66: 180MHz	MCU (Custom PCB Mounted)

3.1.2 SMA wire

The SMA wire sample used in this project was provided by Fort Wayne Metals [62]. The total wire length was $L = 1.0\,\mathrm{m}$ with a diameter $D = 0.3\,\mathrm{mm}$. This SMA sample wire is a commercial product. As such, it is natural to consider the previously mentioned concern regarding the strictly non-linear relationship between the electrical resistance and strain, as mentioned and elaborated in [59, 60].

Despite the research indications and the more complex resistance characteristics exhibited during phase transformation, it is still deemed an exciting prospect of investigation for potential future application. This is especially due to the MRI environment, where silent operation and no AC driving signals provide room for minimizing the adverse signal quality effect normally posed on the MRI system by conventional existing actuators.

Regarding the obtained SMA wire sample by Fort Wayne Metals, certain initial material estimates were provided along with the wire sample. Estimated values for the phase transformation start and finish temperatures for two given constant stress levels. As previously discussed, the stress levels offset the phase transformation temperatures.

TABLE 3.2: SMA wire sample parameter values, [62] Product Development Senior Engineer Wayne Buchan

Axial Stress / Transformation Phase	A_s	M_f	M_s	A_f
$100\,\mathrm{MPa}$	$\approx 47\,°\mathrm{C}$	$\approx 42\,°\mathrm{C}$	$\approx 74\,°\mathrm{C}$	$\approx 79\,°\mathrm{C}$
$150\,\mathrm{MPa}$	$\approx 55\,°\mathrm{C}$	$\approx 50\,°\mathrm{C}$	$\approx 80\,°\mathrm{C}$	$\approx 85\,°\mathrm{C}$
Estimated Recovery Strain ($\%$) at ambient temperature $\approx 20\,°\mathrm{C}$				
$100\,\mathrm{MPa}$	$\approx 4.0\,\%$			
$150\,\mathrm{MPa}$	$\approx 4.4\,\%$			
Estimated SMA wire sample resistivity (ρ)				
$\rho \approx 80\,\mu\Omega * \mathrm{cm}$				

The terms M_s and M_f stand for Martensite start and finish, respectively. Similarly, A_s and A_f are the Austenite start and finish temperatures, respectively. This refers to the estimated temperatures at which the phase transition in the SMA starts and finishes at the indicated stress levels. The recovery strain ($\%$) is an estimate of the SMA wire's ability to return to a complete Martensite phase after a phase transformation has been initiated with heating.

The recovery strain estimate is strictly ideal in the sense that many cycles of temperature annealing under constant stress levels help facilitate the recovery strain as the SMA wire returns to a Martensite phase. Without any added wire stress during this process the SMA wire is not expected to recover nor retain its original sample length for any practical number of repetitions, thus making it unusable.

Furthermore, the recovery strain is indicated as dependant on the ambient temperature. This is due to the connection between phase transformation and temperature in the alloy. Since ambient conditions above a certain level would inherently prohibit the alloy from regaining a full Martensitic state, with passive cooling as the only means of heat dispersion. For the purposes of this project, this is considered as non problematic. The ambient temperature conditions in MRI environments ($\approx$ 19 °C) are strictly controlled and monitored due to the ability to influence patient SAR levels during examination, as mentioned in the section 2.3.4

For the SMA wire, the logical starting point is with the weight and the axial stress. This is calculated by a weight (m) adding tension to the SMA wire of diameter D = 0.3 mm resulting in a constant axial stress (σ) as shown in 3.1.

$$\sigma = \frac{F}{A} = \frac{mg}{\pi r^2} = \frac{mg}{\pi(\frac{D^2}{4})} \tag{3.1}$$

As seen here, calculating the weight (m) from a desired stress σ or vise versa is trivial.

Furthermore, deformation or strain is defined as the ratio of total deformation to the initial condition. In context of the SMA wire, that means the initial length as a full martensitic state, and maximum strain is equal to a full austenite state. General strain equation is shown below in equation 3.2.

$$e = \frac{\Delta L}{L} \tag{3.2}$$

For the SMA wire in a martensitic state (L), ΔL is the wire's length in the austenite state. The strain (e) is expressed as a percentage (%) of contraction in the SMA wire. Lastly, a set of calibrated weights were provided by project supervisor Professor Bjørn Tore Hjertaker ranging from 0.05 Kg-1.0 Kg for accurate axial stress control of the SMA wire.

3.1.3 Test Bench

A test bench was designed and built for the purposes of accommodating potential extra sensors, such as position and temperature sensors. Simultaneously, the test bench is designed to have the ability to exsert a constant stress level on the wire. This was desirable to help facilitate the SMA wire's recovery strain, as two way shape memory effect (TWSME) is practically attained through cycling of the wire hundreds to thousands of times under stress loaded conditions, as pointed out by Senior Engineer Wayne Buchan at Fort Wayne Metals. Another reason was to attempt to map, predict and control the phase transformation onset temperature levels, as these are stress dependant qualities [59, 60].

The test bench was designed using the software Fusion 360, a computer aided design (CAD) program by Autodesk, and made at the mechanical workshop at the Department of Physics and Technology, University of Bergen. The test bench is shown in figures 3.2 and 3.3, below. Figure 3.2 shows a side view of the test bench, while figure 3.3 shows the axle shaft and the weight up close. All relevant test bench items are numbered in both figures, and are listed in table 3.3 for reference.

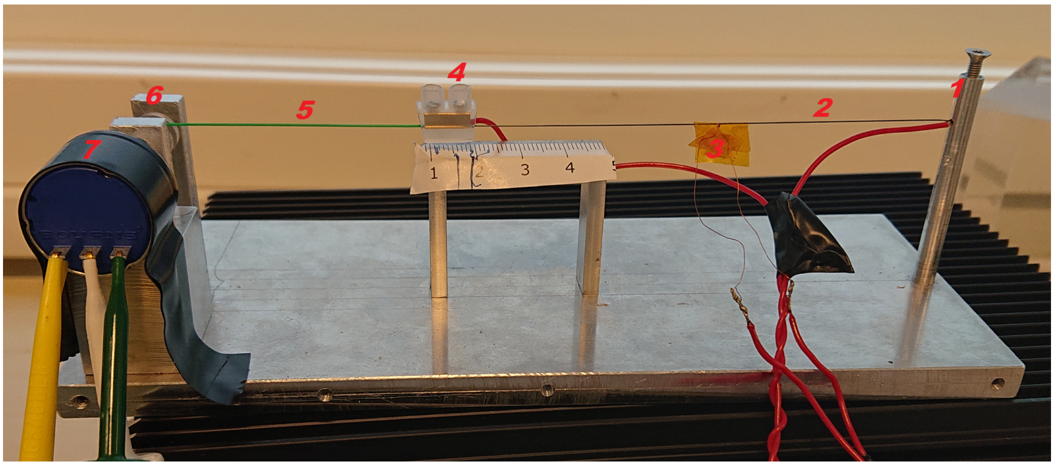

FIGURE 3.2: Test bench setup without cover

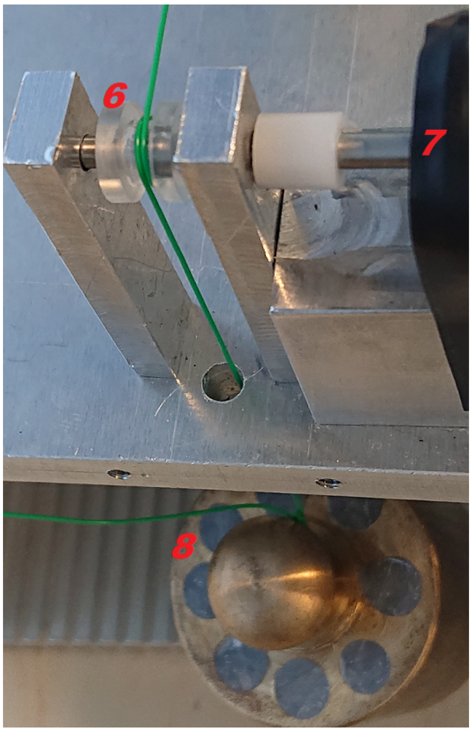

FIGURE 3.3: Test bench setup without cover: front close up view

TABLE 3.3: Test bench Setup: Item description

Item #	***Description***
1	Aluminum Rod with Pinhole
2	SMA Wire provided by Fort Wayne Metals
3	NTC Thermistor (B57540G1 - R/T No.8307)
4	Wire connector
5	Low Weight wire
6	Pulley
7	Rotary encoder
8	Weight

The main design concern with this setup is keeping the rotational friction of the pulley to a minimum under any loading conditions. Hence, the aluminum rod pinhole, diameter $D \approx 1.0\,\mathrm{mm}$, fastening the SMA wire (2) is designed to be at the same height and in line with the pulley wheel. This design choice was intentional in order to minimize the need to account for forces acting along more than two axes. Similarly, the bridge was included as a means of visually detecting the motion of the wire and as a backup in case the position encoder failed. The bridge could also serve as an anchor to attach wires to the setup without adding unnecessary weight which would add to the downwards pull on the wire.

3.1.4 Thermistor

The NTC thermistor [63] was purchased via rs-components.no [64]. The thermistor was the smallest and most reasonably priced sensor available at the time of purchase, with diameter $D = 0.8\,\mathrm{mm} \pm 0.1\,\mathrm{mm}$, see R/T:8307 in data sheet [63]. Worth noting is the relatively large size difference between the diameter of the SMA wire ($D = 0.3\,\mathrm{mm}$) and that of the thermistor.

The effect of the size difference causes accurate temperature measurements to be difficult, as most of the thermistor mass will not be in direct physical contact with the SMA wire as required for optimal measurements. The thermistor was attached to the wire using a polyimide film known as Kapton tape, a highly heat tolerant tape. Since the thermistor is only to be used as an external temperature reference, the sub-optimal measuring conditions were minimized to the best ability, and it is considered as acceptable.

Regardless of the predicted difficulty in temperature measurements, the thermistor was calibrated at the Department of Physics and Technology, University of Bergen.

This was done using two calibration instruments. The Fluke 1586 Super-DAQ Precision Temperature Scanner [65] and the Fluke 9102S dry-well calibrator [66].

The calibration procedure was performed from $20.0\,°C - 60.0\,°C$ with a temperature increase rate of $2.5\,°C/\text{min}$ including stabilization time of 7 minutes at all incremental steps. The Matlab curve fitting tool (cftool) was used to analyse the data, extrapolate values for a new curve fit of range ($10.0\,°C - 80.0\,°C$) and provide corrections to the stated values in the provided data sheet [67].

Figure 3.4 shows the calibration plot, and an associated table 3.4 lists the datasheet provided characteristic constants and the calibrated constants for the temperature sensor.

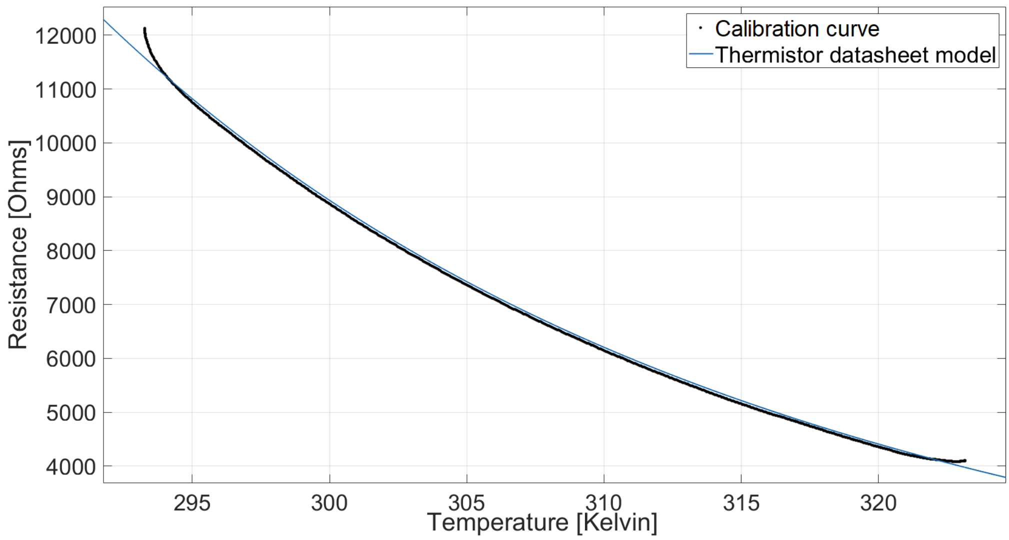

FIGURE 3.4: Matlab - cftool: NTC Thermistor curve fitting

TABLE 3.4: Pre and post calibration constants comparison table

Calibration	**Before**	**After**
β	3492	3388
K	0.08193	0.1111

The reasoning for doing this calibration procedure, despite the fact that the temperature measurement set up itself is somewhat of a flawed premise, was to minimize the error readings to such a degree that the error of the thermistor reading itself is negligible compared to that of the error caused by only partial physical contact with the SMA wire. Regarding the calibration procedure, it is worth pointing out that the range of data for curve fitting was chosen due to match the ambient temperature in an MRI environment, and the expected SMA wire phase transformation temperature. The ambient MRI environment temperatures are $\approx 19\,^{\circ}\mathrm{C}$ [11, 14].

The thermistor in use has a resistance of $10\,\mathrm{K\Omega}$ at $25\,^{\circ}\mathrm{C}$, and follows the exponential resistance model for NTC thermistors shown in equation 3.3.

$$R_\theta = Ke^{-(\dfrac{\beta}{T_\theta})} \tag{3.3}$$

R_θ is the resistance at degree Kelvin, K and β are constants for a given thermistor with values found in the datasheet [67], and T_θ is the temperature in Kelvin. The thermistor is set up in a standard voltage divider circuit. A schematic illustration of the voltage divider circuit along with the general equation for obtaining the output voltage of a voltage divider are both shown in figure 3.5 and equation 3.4 respectively, below.

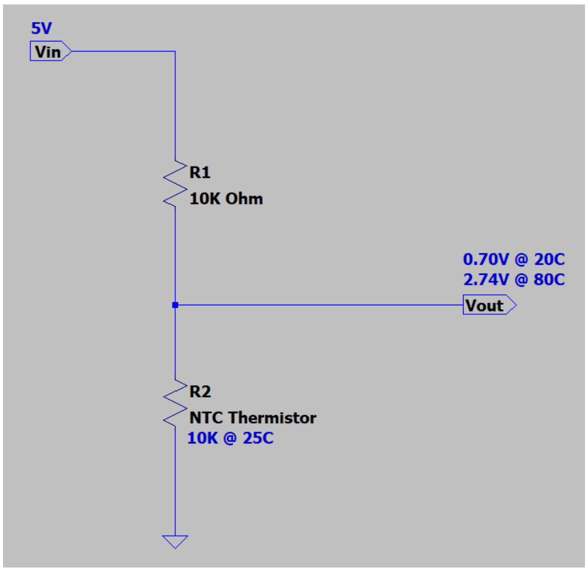

FIGURE 3.5: NTC Thermistor electrical schematic

$$V_{out} = (\frac{R2}{R1 + R2}) * V_{in} \tag{3.4}$$

The circuit is mounted with wires and resistors using the bread board detailed in table 3.1. The output is connected to an ADC on the MCU where it is processed and the temperature calculated based on equations 3.3 and 3.4.

3.1.5 Position encoder

The position encoder [68] was also purchased from rs-components.no [64]. It is effectively a voltage divider with increasing or decreasing analog output depending on clockwise or counter clockwise turning of the axle shaft. The specification number for the purchased encoder "AMS22S5A1BHBFL303" details all the exact technical information and is found in the data sheet [69].

The pulley wheel has the light weight wire wound around it once, as opposed to just hanging over it. This was done as it maximizing the surface contact area between the pulley and the wire, which minimizes potential slippage that would contribute to higher error readings in the position encoder.

In order to convert a rotational motion to linear displacement, arc length is used to model the system 3.5.

$$\mathbf{s} = \theta r \tag{3.5}$$

For our purposes the arc length, **s**, is given by the product of the angle of rotation (θ), in radians, and the radius (r) of the pulley wheel. θ is essentially decided by programmable voltage angle of the position encoder, which is $30°$ or $\approx 0.5236rad$.

The position encoder axle shaft is extended by an aluminum rod on which the pulley wheel is attached. Since the position encoder's axle is effectively turning with the pulley wheel, we can safely use the radius of the pulley wheel in determining the arc length of the system, see equation 3.6.

$$\mathbf{s} = \theta r = \theta \frac{D}{2} = 0.5236rad * \frac{5.71mm}{2} = 1.495\,\mathrm{mm} \approx 1.50\,\mathrm{mm} \tag{3.6}$$

This gives the total range of measurable displacement for the position encoder with the current setup. The estimated measurement uncertainty of this displacement measurement will be addressed in Section 3.1.9, measurement uncertainties.

Comparing the approximate range of measurable displacement to the estimated recovery strain on the SMA wire, taking the stress levels from table 3.2 into account, it is evident that the measurable strain of the position encoder amounts to less than the estimated recovery strain.

$$\mathbf{s}_{measurable} = \frac{\Delta L}{L} \approx \frac{1.50\,\mathrm{mm}}{117.61\,\mathrm{mm}} \approx 0.01275 \approx 1.28\% \tag{3.7}$$

This means that the there is an $\approx$ 3% range in the recovery strain of the SMA wire that is not measurable and also far outside the intended working conditions intended for the SMA wire sample of $\approx 10\,\mathrm{cm}$. The positive aspect of this deliberate design is that the SMA wire will be actuated in ranges where no danger to material fatigue or permanent damage should result due to continuous heat cycling. A decrease in the performance of SMA wire strain ranges have been previously reported [55], due to both overheating and pushing the strain range limits.

The negative aspects include inherently not being able to confirm a full phase transformation, nor being able to observe or measure the full range of the expected resistance change associated with the phase transformation. Regardless, the lack of full range measurable capability is expected and it was decided to proceed with the SMA wire sample of $\approx 10\,\mathrm{cm}$ and the position encoder. The other reason for not choosing a different position encoder was due to availability and pricing of better suited position encoders.

At the time, other available and reasonably priced position encoders had expected output resolutions of 12-Bit over $330° - 360°$, compared to the chosen position encoder with a 12-Bit at $30°$ deflection. Another position encoders had a too coarse resolution capability, and would make it difficult to accurately determine displacements on the order of $\pm 0.05\,\mathrm{mm}$. Since the possible integration with NNL's MRI compatible visual system high definition (VSHD) goggles is a motivating factor in this project, and the measurable displacement range was within reasonable margins, it was decided to proceed.

Moving on, the position encoder itself has three terminals, working as an internal voltage divider. This ranges from $0.0\,\mathrm{V} - 5.0\,\mathrm{V}$, with 12-bit resolution at the pre programmed angle ($30°$) and has recommended load resistance $R_L = 10\,\mathrm{K\Omega} \to \infty$. Similarly to the NTC thermistor measurement circuit in figure 3.5, the same strategy was applied to the measurement circuit for the position encoder. However, due to the custom PCB by NNL, the ADC available on the MCU has a $3.3\,\mathrm{V}$ input.

This meant having to slightly modify the voltage divider circuit so the full input range for the ADC could be used. The circuit schematic is shown in figure 3.6 and the modification to equation 3.4 is detailed in equation 3.8.

$$V_{out} = (\frac{R3}{R1 + R2 + R3})V_{in} \tag{3.8}$$

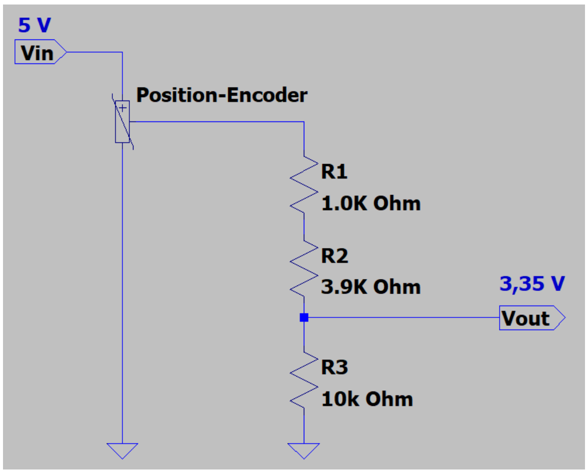

FIGURE 3.6: Position encoder electrical schematic

3.1.6 Magnetic interface unit and power supply

The K66 Cortex-M4F micro controller (MCU) is integrated on a printed circuit board (PCB) known as the Magnetic Interface Unit (MIU), designed by NNL. Its function is to power the MRI compatible VSHD goggles by NNL [70]. The MIU board is part of the power supply for the VSHD goggles. It contains several DC-DC converters and has to be placed in a remote shielded location from the MRI scanner due to noise generation. It supplies power to the VSHD goggles via shielded cable. Hence, the MIU integration into the experiment for monitoring and control represents the first step of integration with NNL's VSHD goggle system. Therefore, the integrated K66 Cortex M4F MCU was the logical choice of controller for the project.

Table 3.1 lists the equipment of two separate power supply units (PSU). Due to the fact that the Toellner Toe 8735 is analog, it does not provide very accurate currents. It is therefore only used to power the RH-74 bread board, the NTC thermistor and the rotary encoder listed in table 3.3. The EA-PS 2042-06B PSU is digital and has computer interface capabilities. This allows for a controlled and more precise and stable supply current. As ohmic heating is the actuation facilitator, it is essential to have a very accurate and stable supply of current for control purposes. The PSU is used to provide power to the SMA wire.

Additionally, the system power values and resistance of the SMA wire are both calculated on the MCU from the voltage and current values logged by the EA-PS 2042-06B PSU. This was the most convenient way to obtain the resistance for the system while being powered, at least for the case when the wire is directly connected to the power supply. For different setups the supplied power is still easily obtained from the supplied voltage and current values, and such, remains a valuable source of data acquisition regardless of experimental setup changes. Other potential resistance measurements will be addressed in their respective sections.

3.1.7 Software and embedded system

The MCU and the EA-PS 2042-06B PSU are both programmed using C++ in an integrated development environment (IDE). The software(s) used are MCUXpresso IDE for the MCU and Code::Blocks open source IDE for the PSU. A J-link debugger probe is used upload the MCU program to the MCU via a USB port. The created software programs were initially provided in skeleton form by co-supervisor and NNL Senior Hardware Developer Olav Birkeland to facilitate the starting process of programming the MCU and controlling the PSU. Both the MCU program and the PSU control program were thereby further modified and developed in the project, with some assistance by co-supervisor Olav Birkeland during encountered difficulties.

MCUXpresso was the IDE of choice for programming the MCU and for finalizing the MCU program. This was chosen since MCUXpresso is supported by NXP semiconductors, the company currently in charge of all of Kinetis K family MCUs. Similarly, Code::Blocks was chosen as the IDE for the further development and modification of the PSU control program because the skeleton structure had already been prepared in Code::Blocks by co-supervisor Olav Birkeland.

In order to circumvent clock differences in data logging, the MCU program and the PSU control program are both initialized through the Code::Blocks IDE. When initialized, a configurable pre-programmed sequence is executed, fully controlling the current delivery and also responsible for recording all measurements for the system. Upon sequence end, the program automatically saves the data to a file for later analysis.

The MCU is connected to the computer via a USB interface running on a virtual COM port (VCOM). The VCOM communication protocol was integrated into the PSU control program from a skeleton tutorial VCOM code example provided with the Code::Blocks IDE software. The VCOM protocol is configured to receive and process the thermistor and position encoder data through the PSU control program as a data string, which is formatted and transmitted by the MCU program. The received string is subsequently reformatted to numeral values and interpreted as measurements. These measurements are then usable as parameters by the PSU control program in controlling the input currents.

The EA-PS 2042-06B PSU is controlled remotely via a USB port, and has a multitude of different configurations and settings. The relevant controls and features for the PSU control program are configurable via the Code::Blocks IDE, and include setting for voltage, current, overvoltage (OVP) and overcurrent (OCP) protection. The OCP and OVP provides good redundancy for overheat protection during experiments. Additional settings include a toggle for constant voltage (CV) or constant current (CC) mode. The ability to preset either a CV or CC mode for power delivery is vital to the prevention of overheating for this type of system. Since the wire resistance varies with temperature, not actively using a constant current feed has the very likely potential of causing spikes of high current surges in the power delivery. This can cause permanent damage and alter or destroy the TWSME capabilities and the recovery strain of the SMA wire. This effect was also cautioned by Fort Wayne Metals Senior Engineer Wayne Buchan.

3.1.8 ADC

The MCU has two 16-bit ADC modules, ADC0 and ADC1, both with $3.3\,\mathrm{V}$ inputs. They are both configured to 12-bit for all experiments. The overall reasoning for this is strictly due to not having a precise enough setup to require a 16-bit precision. ADC0 is responsible for the position encoder, while ADC1 is responsible for the thermistor. Both ADC modules are located in the MCU on the MIU board, with inputs for the ADC modules accessible from points on the MIU board. These points were identified from NNL PCB schematics for the MIU board. Schematic cutout of the ADC input circuits are included in figure 3.7.

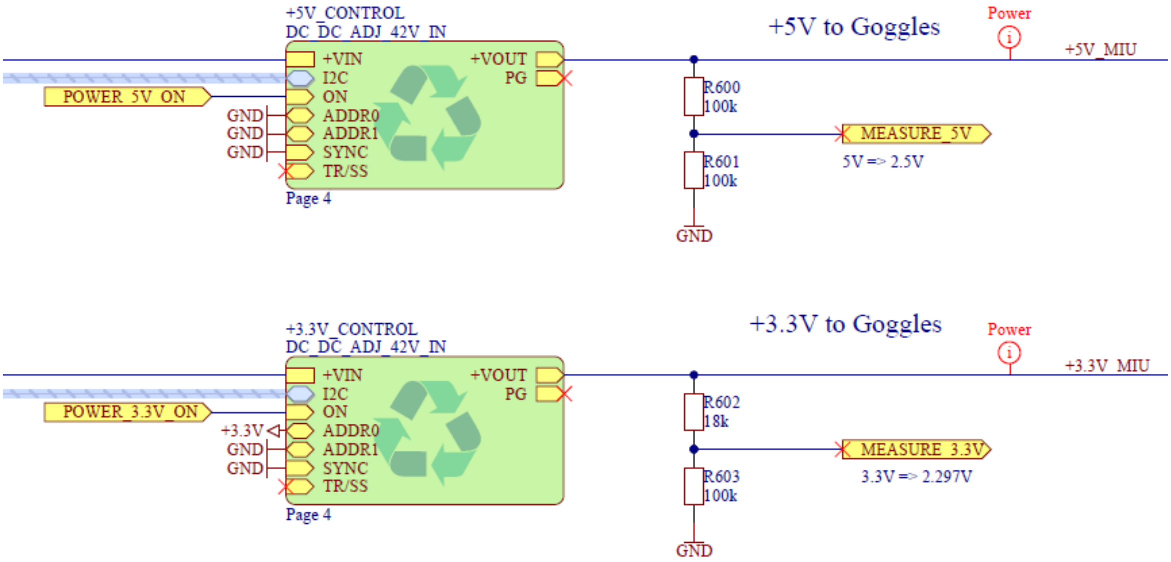

FIGURE 3.7: MIU: ADC input circuits

Additionally, the MCU pin schematic details the configuration for ADC input pins, this is also included in figure 3.8.

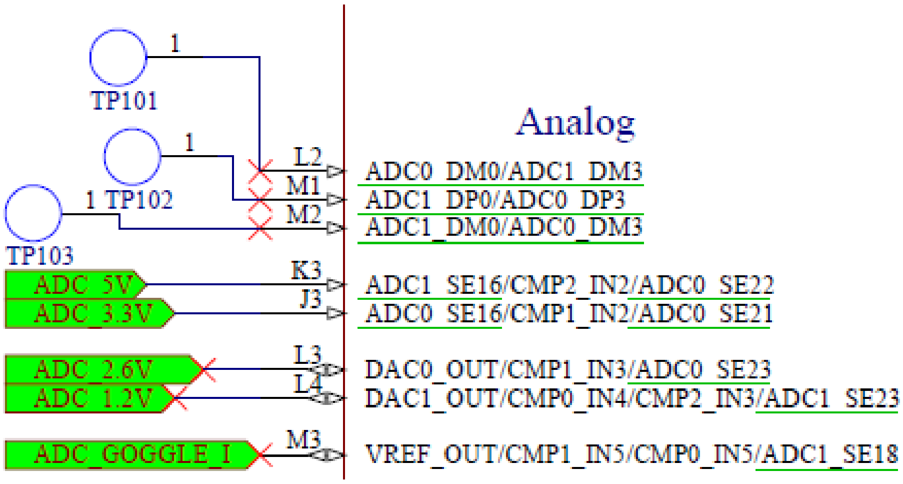

FIGURE 3.8: Setup of the MIU: MCU, ADC and DAC input output pin configuration

The MIU and MCU schematics are provided by courtesy of co-supervisor Olav Birkeland. The MIU board was reconfigured for use with external lead wires. This was done by directly soldering the lead wires onto the board. A total of four soldered lead wires, for two corresponding ADC inputs and two DAC output modules for future potential use.

The ADC modules are configured for single ended input. The signal sources are located near the ADC modules themselves, with no significant noise sources present, apart from the fact that the circuitry is connected on a bread board. Additionally, both ADC modules are configured to output an average of the last 8 sample values, this is mainly to get smoother and less spiky readings.

The thermistor, figure 3.5, is connected to ADC1. The output voltage of the measurement circuit was designed to use as much of the signal range as possible, considering the available components, which is $\approx 0.70\,\mathrm{V}$ at $20\,^{\circ}\mathrm{C}$ and $\approx 2.74\,\mathrm{V}$ at $80\,^{\circ}\mathrm{C}$. Following the digitization of the voltage signal, the voltage signal conditioning by the MCU is primarily done through equations 3.3 and 3.4. The values are then transmitted as data string values via the VCOM interface to the computer, where it is read and further used in PSU control program.

The position encoder output, figure 3.6, serves as input for ADC0. As mentioned in the section on the position encoder, it works as a voltage divider with 12-bit resolution at the pre programmed angle of $30°$, equalling $\frac{3.3\,\mathrm{V}}{30°} = 110\,\mathrm{mV}/1°$. Similarly, the output resolution specified in [69] for the ADC can be expressed as $\frac{3.3\,\mathrm{V}}{2^{12}} \approx 0.81\,\mathrm{mV}/bit$. Together, they form the relationship expressed in equation 3.9.

$$ADC0_{input} = 110\,\mathrm{mV}/1° \approx 0.81\,\mathrm{mV}/bit \longrightarrow ADC0_{output} \approx 0.81\,\mathrm{mV}{*}136bits = 110.16\,\mathrm{mV} \tag{3.9}$$

Equation 3.9 is an estimated calculation of the number of steps of the ADC_{output} that equates to a displacement of $1°$ deflection of the position encoder. By using the estimated voltage for angular deflection obtained from equation 3.9, it is trivial to input for the angle in the arc length equation, 3.5 to obtain the linear displacement of the system.

3.1.9 Measurement uncertainties

Determining the uncertainties in the measurement setup detailed above is no simple task. More often than not, there are magnitudes of differences in weight factor. As such, this section will entail the different uncertainty elements pertaining to instruments used directly in the test setup and the constituent elements involved in the experiments.

Starting with the power supplies, the Toellner TOE 8735, datasheet [71], is used to power the breadboard connector circuits with a constant supply of $5.0\,\mathrm{V}$ and $30\,\mathrm{mA}$ for continuous use of both circuits, figures 3.5 and 3.6. The fluctuations in constant voltage mode, provided the PSU stays powered on for more than 10 minutes prior to actual measurement start is marginal at best, and is considered to be of minimal significant impact.

The EA-PS 2042-06B datasheet [72], is used to power the SMA wire and is of higher importance. The voltage fluctuation is stated at 0.2% for the used model, which equals a small but potentially significant factor if the PSU would be considered to be used in a high precision setup, the current has the same accuracy specifications of 0.2%. Considering that the current is by far the most important factor in ohmic heating, it could well be that the current fluctuations will affect the stability of the measurements once a desired level of strain is reached for the wire. This, however, will be determined and referenced vs the position encoder accuracy in order to determine dominant instability factors.

The thermistor measurement uncertainty is, as discussed in the thermistor section, not a dominant factor in the overall temperature reading of the SMA wire. This is due to the size difference causing only partial physical contact between the thermistor and the SMA wire. The calibration procedure performed on the thermistor effectively puts it at $\leq 0.2\,°\mathrm{C}$ accuracy, which is lower than the measured temperature accuracy of the SMA wire due to the partial physical contact. As such, temperatures are difficult to estimate, but an initial uncertainty of $\pm 2.0\,°\mathrm{C}$ are assumed to be within a reasonable error margin.

The position encoder has a several measurement uncertainties that needs to be taken into account. Environmental, mechanical and electrical characteristics are all stated in the datasheet [69] with the characteristic of the most importance being discussed here.

For the electrical, the output voltage accuracy of the position encoder is stated at $\pm 1\%$ V_{DD} which is $50\,\mathrm{mV}$ at $V_{DD} = 5.0\,\mathrm{V}$. The proportionality between the mechanical angle and the output voltage or, the independent linearity, is stated at $\pm 0.5\%$, which is $0.15°$, or $16.5\,\mathrm{mV}$ in measurable voltage. Finally, the hysteresis at a maximum of 0.02% V_{DD} which is $10\,\mathrm{mV}$. Combining this with the numbers presented in the ADC, Section 3.1.8, it is evident that these factors contribute to an overall measurement uncertainty of $\approx 0.7°$ of the mechanical angle. Stated in terms of linear displacement $\approx 0.7°$ equates to $\approx 0.05\,\mathrm{mm}$, as calculated from equation

3.5, using $\Theta = 0.7^\circ$ and $r = \frac{D}{2}$ of the position encoder axle shaft. This approximate measurement uncertainty is the estimated uncertainty in the measurable linear displacement as calculated from equations 3.6 and 3.9. The linear displacement equation provided above in Section 3.1.5 is here reiterated including the estimated measurement uncertainty.

$$\mathbf{s} = \theta r = \theta\frac{D}{2} = 0.5236 rad * \frac{5.71mm}{2} = 1.495\,\mathrm{mm} \approx 1.50\,\mathrm{mm} \pm 0.05\,\mathrm{mm} \tag{3.10}$$

This of course does not account for the repeatability and stability of the positioning, as the heating of the wire and dissipation of heat further complicates the issue and would require a more controlled environment and many cycles to establish firm statistical data for confirmation.

Adding to the above, the fact that the circuit is present on a breadboard, and some extra leeway due to indeterminate factors such as resistor tolerance variations, conductor loss and banana plug connectors. The estimation stated in equations 3.6 and 3.9 is erring on the cautions side. Nevertheless not inaccurate enough to be considered theoretically unrealistic for the experimental setup.

For the mechanical parts of the position encoder, the diameter of the encoders axle shaft is $D \approx 3.18\,\mathrm{mm}$, and is connected to a pulley wheel of diameter $D \approx 5.71\,\mathrm{mm}$. Both checked and measured with digital calipers, which has a noted accuracy of $\pm 0.03\,\mathrm{mm}$ [73]. The caliper was used to measure the diameter of the pulley wheel for fitting it to the axle shaft. Furthermore, the axle is connected aluminum rod to the attached pulley wheel and the two rotation anchor points on the test bench provide an overall increase to the systems friction and moment of inertia. These points are however neglected for the purposes of this experiment. To initiate rotation of the position encoder axle there needs to be some mechanical resistance, otherwise relative position determination would prove extremely difficult. However, it was of high importance that the position encoder inherently required as little force as possible, in order to be able to measure sub millimeter displacements with low mechanical resistance.

Regarding the added bridge on the test bench, figure 3.2. The total measurable displacement of the position encoder amounts to $< 2\%$ of the total estimated strain achievable on an $\approx 10\,\mathrm{cm}$ SMA wire. It is difficult to quantify the exact position during full phase transformation. As such, attempts were made to estimate this by attaching a measuring tape to the bridge on the test bench. The noted relative position of the connector between the SMA wire and the weight wire are recorded with a thin pen before and after relative motion stop of the wire.

This was done throughout a maximum current and passive cooling experiment, and is a test specifically designed to put the SMA wire in a complete Austenite phase transformed state to observe passive the cooling rate. The measuring tape pen markings were measured with digital calipers a total of 10 times with an average length of $\approx 3.75\,\mathrm{mm} \pm 0.03\,\mathrm{mm}$. In conclusion, the measuring tape is a crude measuring reference value which does not allow for a true maximum strain measurement. Taking caliper measurements of markings on the tape, however, does provide a more accurate reference to the total displacement posed by complete phase transformation, which is valuable information.

Chapter 4

Results and discussion

4.1 System characterization

As an experimental starting point, a characterization of the SMA wire based on new experimental data is required. The SMA wire provided by Fort Wayne Metals is a commercial product and not specifically produced for this project. Therefore, possible deviations and differences in the alloy itself may prove incompatible when compared with existing research. It also serves an equally important purpose, i.e. to determine and verify limits of functionality, accuracy, repeatability using the designed measurement setup. Worth noting, it is recognized and expected that the experiments will only provide initial characterization data.

The system characterization has several objectives:

1.) Hysteresis behavior observation.

2.) Heating and cooling response time determination.

3.) Resistance and displacement mapping.

4.) Resistance and displacement relationship analysis.

For all the tests in these series of measurements, the EA-PS 2042-06B PSU is connected directly to the SMA wire sample. Regarding the following measurements and figures; due to the limited range of the position encoder used it is not possible to map the complete range of phase transformation and consequently, see section on the position encoder and equation 3.7.

Hence, the start and finish temperatures for the respective Austenite and Martensite phases (As, Af and Ms, Mf) are used to refer to the start and finish temperatures of the relative measurement series performed. These are not to be confused with the context of absolute phase transformation. This applies to all references to start and finish temperatures for the performed experiments, unless otherwise explicitly stated.

4.1.1 Hysteresis testing

The first experiment serves as a test for the basic and most well known documented characteristic of SMA materials. The hysteresis relationship between wire temperature, strain and resistance during heating and cooling.

A point of contention regarding the data represented in this section in relation to previous research. The traditional representation of the SMA hysteresis relationship has been between temperature and strain. However, a conscious choice is made here to directly use displacement as a measured quantity as opposed to strain. Strain is a percentage based quantity, whilst displacement is shown in units of millimeter. The basic for this choice is simple, the resultant error calculations, whether based on statistics or model calculations, would be visually misrepresented if strain is to be used directly for plotting, given the fact that the measurable strain range is estimated at $\leq 2\,\%$. Displacement was therefore pragmatically chosen as it provides a better visual indication as opposed to a $1-2\%$ scale.

The measurements in this first test was performed as follows. The PSU was programmed to supply a CC while automatically adjusting the required voltage up to a max. The constant current was increased incrementally at a rate of $\approx\ 10\,\mathrm{mA/s}$ in 80 steps up and down, respectively. OVP was set to $2.0\,\mathrm{V}$ and OCP to $900\,\mathrm{mA}$. This allowed for a slow increase of supplied power to the SMA wire, with ample time for the measuring circuitry to record position and relative temperature increases. At the same time, allowing the PSU and wire a few hundred milliseconds to stabilize in between changes. The plotted data is an average of 10 independent series of measurements with the same initial settings. The error in relative displacement is included as the standard deviation for the measured data sets. The SMA wire sample under testing is subjected to a constant stress ($\sigma \approx 138.8\,\mathrm{MPa}$), as calculated by equation 3.1 using a $1.0\,\mathrm{kg}$ weight.

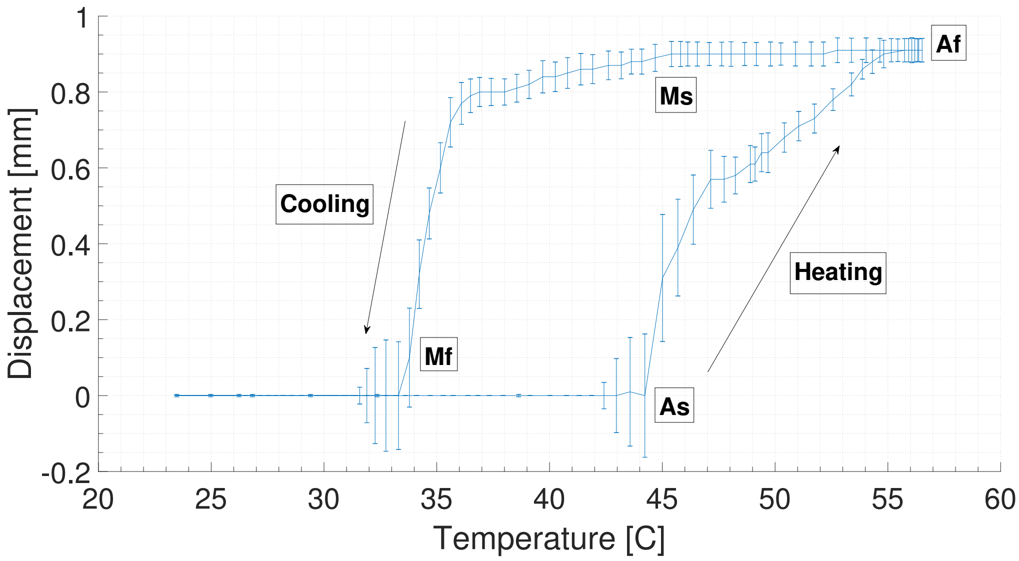

FIGURE 4.1: Temperature-displacement relationship

The hysteresis between the heating and cooling phases are clearly visible and separated beyond any uncertainties for the measurement system. This confirms the hysteresis behavior between temperature and strain for this commercial SMA wire sample, similarly observed and reported in previous research [55, 56, 57, 58, 60]. Subsequently, attempts were made to observe similar hysteresis behavior in the resistance of the SMA wire for the same data series. The expected observation is the same hysteresis behavior when plotting the calculated wire resistance from the PSU recorded values against the measured temperature.

For this purpose, an initially theoretical measurement uncertainty calculation for the resistance based on the PSU datasheet [72] and Ohm's law was formulated. Results when overlaying this uncertainty on one randomly selected series are shown in figure 4.2 for illustrative purposes.

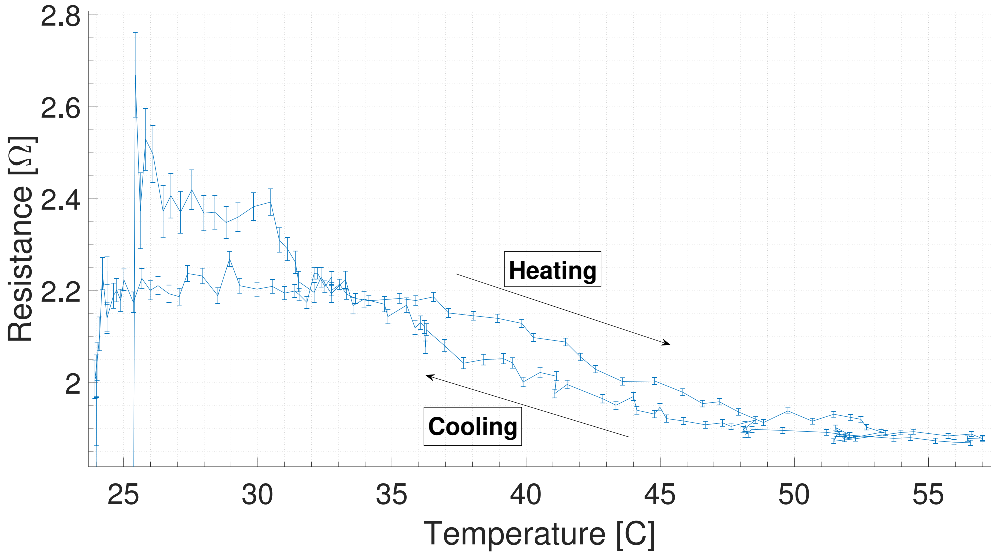

FIGURE 4.2: Temperature-resistance single series hysteresis

This result from a single cycle of heating and cooling shows expected hysteresis within margins of the theoretically calculated measurement uncertainty. However, when plotting all performed measurement series as mean values with errorbars for the corresponding data set variations, figure 4.3, it is evident that the measurements show too much variation and overlap to be able to conclude a definite hysteresis behavior.

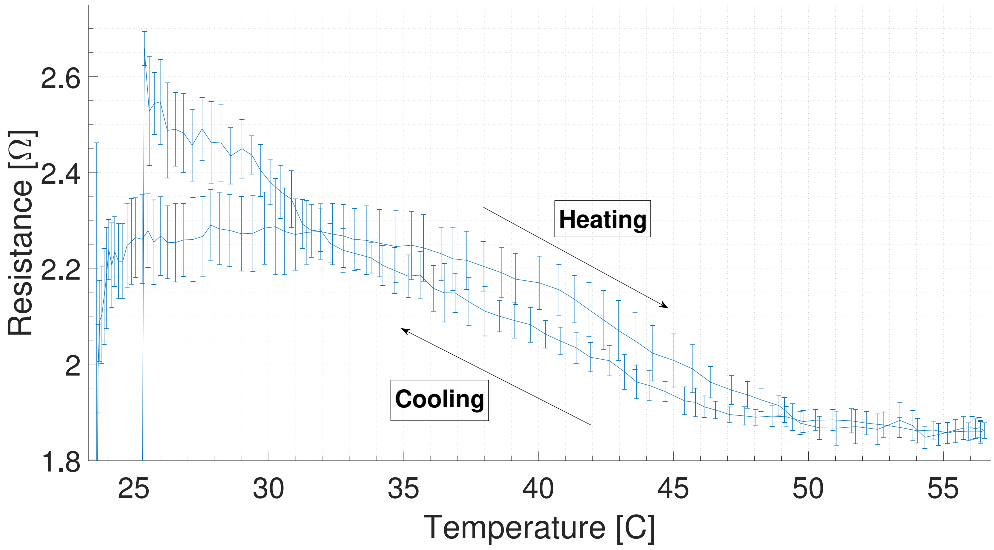

FIGURE 4.3: Temperature-resistance hysteresis

This is most likely due to the PSU, more so than any deviations in the SMA wire material. The PSU may simply not be able to provide accurate enough voltages and/or currents for this project's purpose. It is entirely possible that the PSU has a too coarse precision supply of voltage and current, all though operating in CC mode, the voltage supply level jumps are too high for the subtle resistance changes the SMA wire undergoes. Add to this banana plug connectors and partially exposed lead wires to the SMA wire, it does not constitute the ideal platform for sensitive resistance measurements. It is worth noting that the errorbars representing the deviation shown in figure 4.3 vary by $\approx 200\,\mathrm{m}\Omega$. This is a relatively low resistance deviation in on itself. However, the only clear observable information drawn from figure 4.3 is, as temperature increases the resistance decreases, with possible hysteresis behavior observed during cycling.

Plotting the measured displacement and resistance data vs time instead of temperature. This is useful because it allows us to identify points in sequenced time when behaviors coincide. An example is shown in figure 4.4 below at the onset of detected displacement by the position encoder. This is overlapped by the same resistance readings taken for comparative reasons.

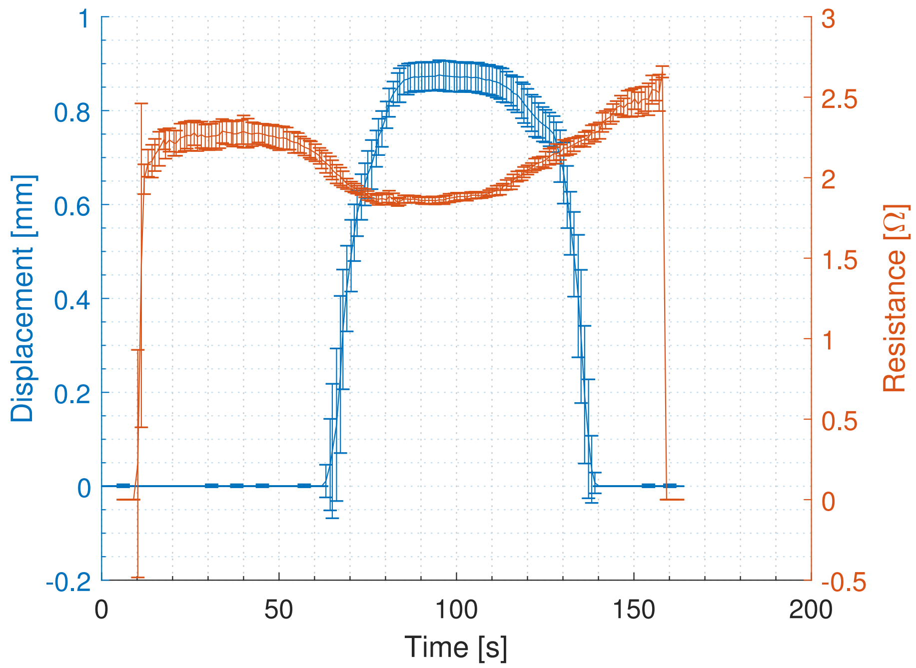

FIGURE 4.4: Displacement and resistance vs time

Observed here are the onsets of resistance change along with the displacement change as functions of time. It is clear from the overall behavior that a resistance change precipitates the phase transformation of the SMA wire. This might however seem self evident, as the resistance turns towards lower values as temperature increases. Lastly, the one conclusion to be drawn from the initial measurements presented is that it supports the existing hysteresis behaviors of Nitinol SMA wires observed in previous research [55, 56, 58, 60].

4.1.2 Heating and cooling response time testing

For testing the passive cooling capabilities of the SMA wire, the test bench was enclosed in a plexiglass cover to minimize airflow around the wire. The SMA wire was then supplied with a pre decided maximum current output of $900\,\mathrm{mA}$ from the PSU.

This maximum current output was decided partly due to considerations made by Senior Engineer Wayne Buchan at Fort Wayne Metals, and from wanting to stay below $1.0\,\mathrm{A}$ for all experiments. A key factor for the decision to limit current, and thus overall power, is due to restrictions in potential compartment size for future integration with NNL hardware and the available power supply on existing NNL hardware.

The first test in this experiment was designed to apply the maximum current for a period of $100\,\mathrm{sec}$ then monitor the temperature and the displacement for $400\,\mathrm{sec}$. This was done to map the passive cooling time and the free recovery strain of the wire. This was performed a total of 5 times for repeatability and to establish some statistical data. The results are represented with averages of these measurement series.

Additionally, a rough measurement of the total displacement range and thus strain of the SMA wire was also allowed by this test, by the measuring tape fastened to the test bench bridge. Below is a plot of the measured displacement and temperatures taken during the test(s).

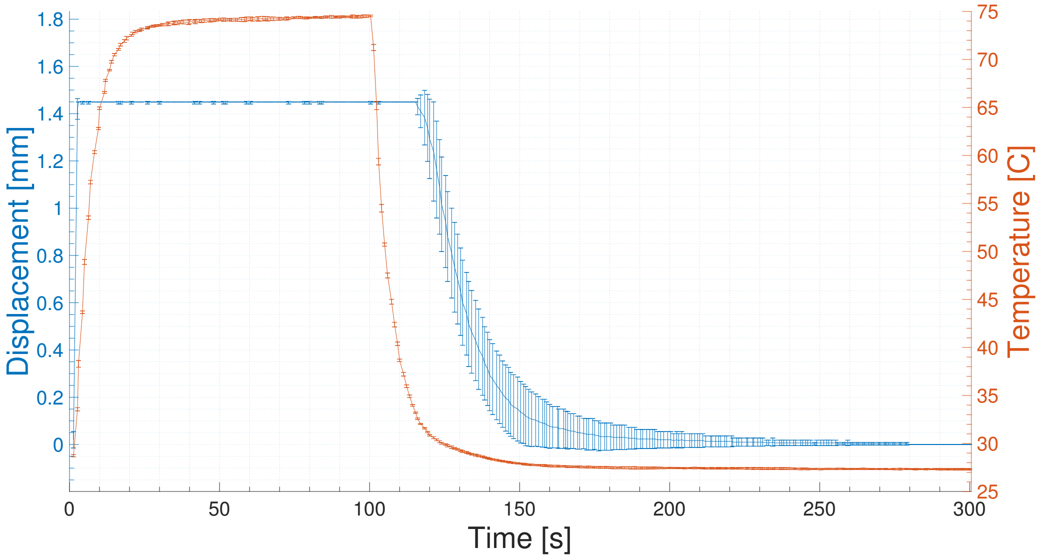

FIGURE 4.5: Maximum heating and passive cooling

One thing evident from the plot is that the SMA wire will go to maximum measured displacement levels very quickly following the onset of the set maximum current of $900\,\mathrm{mA}$. It reaches peak measurable displacement after $3\,\mathrm{sec}$. Further observations of the wire connector during the test showed maximum displacement reached shortly thereafter, as measured by markings on a measuring tape, mentioned above in Section 3.1.9 measurement uncertainty. Estimations on the heating and cooling rates can also be made from figure 4.5.

The estimated heating time from figure 4.5 is $\approx 15\,\mathrm{sec}$ from $\approx 25\,°\mathrm{C}$ to $\geq 70\,°\mathrm{C}$ and $\approx 33\,\mathrm{sec}$ to $\approx 74\,°\mathrm{C}$. These provide two rough estimates on heating rates, see equations 4.1 and 4.2, respectively.

$$\frac{\delta T_{25C}^{70C}}{\delta t} \approx 3\,°\mathrm{C}/\mathrm{sec} \tag{4.1}$$

$$\frac{\delta T_{70C}^{74C}}{\delta t} \approx 0.12\,°\mathrm{C}/\mathrm{sec} \tag{4.2}$$

Additionally, the supplied current throughout the experiment was $I \approx 900\,\mathrm{mA}$, with an average voltage of $V \approx 1.57\,\mathrm{V}$. The power required for these heating rates are the same, and is given by $P = IV \approx 1.41\,\mathrm{W}$.

For the cooling time, after switching the current off at $100\,\mathrm{sec}$, it takes $\approx 23\,\mathrm{sec}$ to reach $\approx 30\,°\mathrm{C}$, and another $27\,\mathrm{sec}$ to $< 28\,°\mathrm{C}$. Worth noting, the ambient temperature measuring during the day of this experiment was $\approx 27.5\,°\mathrm{C}$, which is the reason for the extra slow heat dissipation rate as the SMA wire temperature approaches ambient. This provides the corresponding estimates on the two cooling rates, see equations 4.3 and 4.4, respectively.

$$\frac{\delta T_{74C}^{30C}}{\delta t} \approx 1.91\,^{\circ}\mathrm{C/sec} \tag{4.3}$$

$$\frac{\delta T_{30C}^{28C}}{\delta t} \approx 0.07\,^{\circ}\mathrm{C/sec} \tag{4.4}$$

Furthermore, looking at figure 4.5, there is an apparent delay between the response of the displacement and the temperature. Given the position encoder's mentioned measurement range being saturated at $\approx 1.45\,\mathrm{mm}$ it is an expected and explainable behavior. As such, the first noticed decreasing displacement value is noted at $\approx 116\,\mathrm{sec}$. From this position to a complete return transformation to Martensite phase the elapsed time is $\approx 65\,\mathrm{sec}$, adding to that another $10\,\mathrm{sec}$ before a noticable decrease in the deviations of the measurements become apparent.

A total of at least $100\,\mathrm{sec}$ for a complete return transformation, and reset of position initial conditions is the limit of this system under the stated experimental conditions. As mentioned in section 2.4.4. a major drawback to SMA materials are slow response times. This is clearly evident based on the obtained results. Passive cooling by power shut off and natural convection is determined to a large degree by the relative temperature difference between the wire and ambient conditions.

4.1.3 Resistance and displacement mapping

The majority of research into SMA based actuators have revolved around employing some form of resistance positioning feedback. The reason for choosing resistance feedback, as opposed to temperature feedback, has traditionally been the reported simplified linear relationship between the electrical resistance and material strain during phase transformation.

As previously mentioned, this is strictly not the case for commercially available SMA wires. For this project however, this issue could potentially be mitigated. Reasons for this are the limited phase transformation of the SMA wire and the restricted ambient temperature limit posed by the conventional MRI environment. This however, requires further testing.

A foreseeable problem with the current experimental setup regarding resistance measurements were already encountered when documenting the hysteresis behavior, see figure 4.3. Another challenging issue concerns the provided material specifications by Fort Wayne Metals, see tab 3.2. Given the SMA wire sample resistivity of $\rho \approx 80\,\mu\Omega/\mathrm{cm}$, the expected resistance for SMA wire sample 1 should be in the range of $\approx 1.0\,\mathrm{m}\Omega$ at best. Fort Wayne Metals was enquired about this, but no additional information regarding the resistivity was obtained. However, it only serves to note this unexplained discrepancy. The calculated resistance value available from measurements is the value that has to be documented and considered.

The first experiment performed for the purpose of mapping the resistance behavior was a series of measurements in increasing increments of $100\,\mathrm{mA}$ up to the point where the position encoder started detecting significant motion. After the detection limits were established, a lower increment of $10\,\mathrm{mA}$ was set to test for position and resistance differences under small but manageable increases of current load.

All steps were measured in 6 independent series, each over a $400\,\mathrm{sec}$ time period. This was done to obtain a small statistical data set to characterize the stability and repeatability in the positioning of the system at small current differences. Figures 4.6 and 4.7 shows the displacement and the resistance as a function of time, respectively.

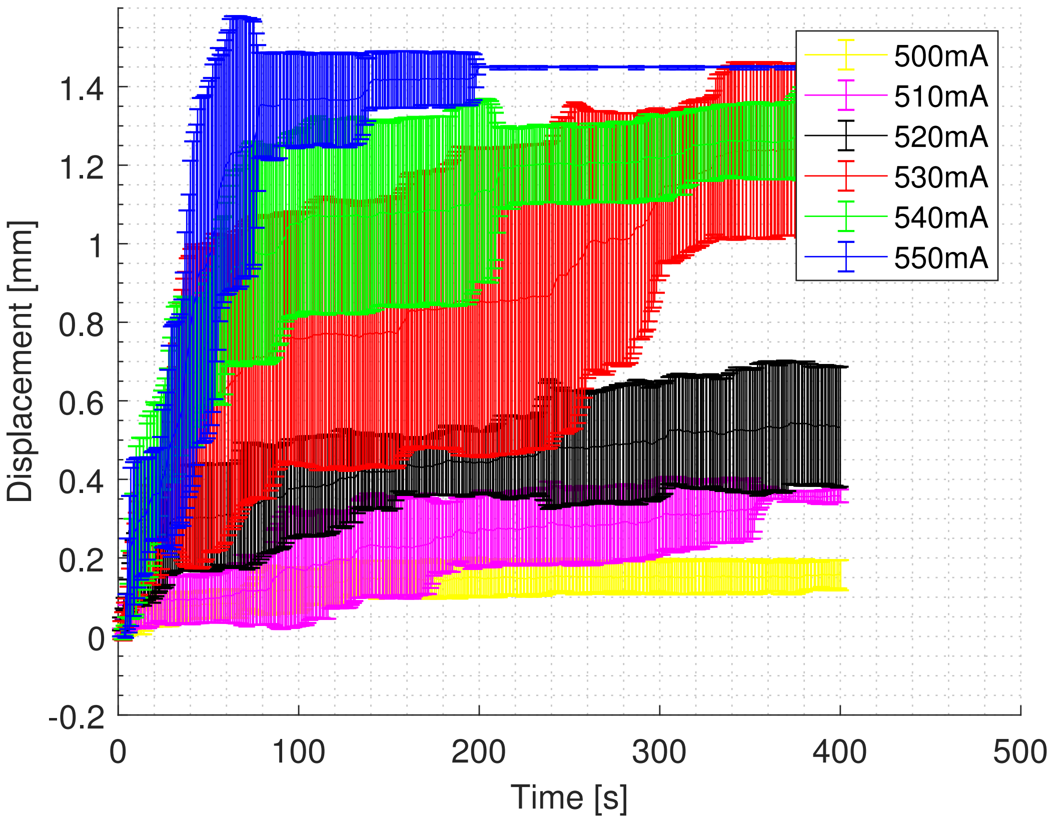

FIGURE 4.6: Displacement at different input currents

From figure 4.6 it is clear that any input current of $\geq 510\,\mathrm{mA}$ supplied to the SMA wire will provide significant displacement. There is no definite separation in positioning based solely on current input, even over time. Unfortunately for stability and repeatability, there is too large a variation in positioning despite the long sampling window and the relative stability of the supplied current. Two possibilities for this are rougher commercial production methods and again the PSU used for these experiments not being accurate enough. The former possibility supports previous observations [59, 60]. The experimental setup used in [59] employed a MOSFET transistor with power modulation to supply current to the SMA wire. This inherently allows for greater control and stability as opposed to the programmable PSU used for this project.

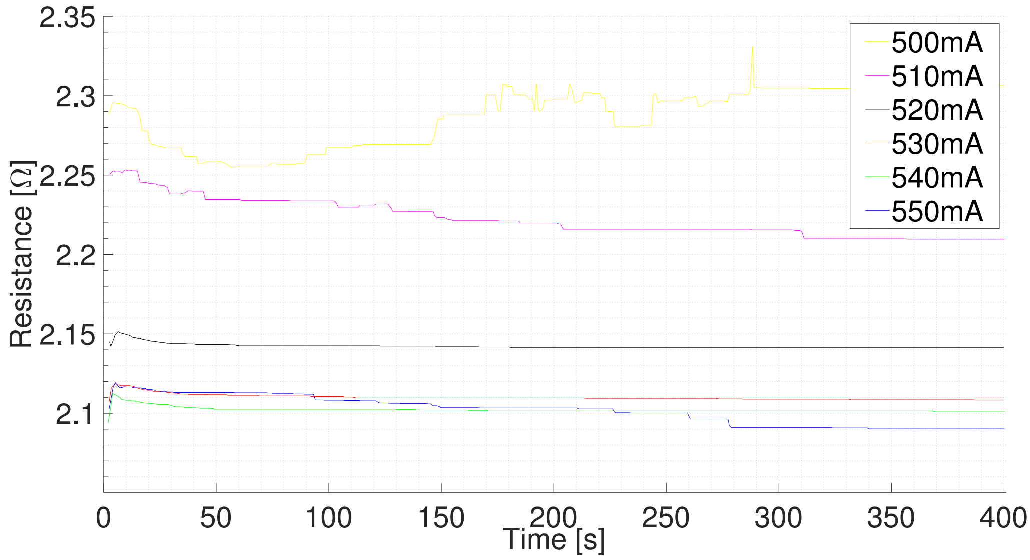

FIGURE 4.7: Resistance trends at different input currents

Furthermore, figure 4.7 shows the resistance trends at different current input levels. The errorbars have been left out for illustrative purposes. As figure 4.6 clearly shows a large variation in the spread of data, and it would only serve to mask observables in this case. Despite the large data variation, there is still an observable trend that conforms with previous findings regarding SMA material behavior, this is the decrease in electrical resistance as the SMA wire undergoes phase transformation from Martensitic to Austenite form. The incremental increasing supply current plots show that the trend behavior is indeed indicative of a decreasing electrical resistance as the wire undergoes phase transformation. However, the data sets remain too varied for more than a general observation.

It is clear that a more optimal way of measuring the SMA wire resistance is required. The resistance variation calculations obtained thus far by using the PSU voltage and current values are not enough to detect changes on a scale of $\approx 100\,\mathrm{m\Omega}$. There is simply too much statistical variation over repeated testing, clearly illustrated by the data spread.

4.1.4 Resistance and displacement relationship analysis

Despite the large variation shown in repeated testing, the resistance and displacement data mapping attempts provide an opportunity to further analyse the relationship between the resistance and displacement. Any new system design development requires a confirmation of whether or not existing observational behavior are to be expected or not.

As such, attempting to characterize the observed, yet simplified, linear relationship is of importance to this project in terms of control viability moving forward. Worth noting also is that the data is of interest for comparison purposes with future measurements.

The analysis is made on each of the 6 measurement series, detailed in Section 3.2.3. Before proceeding with the curve fitting analysis of the individual data series, an overall plot detailing all measurements are presented. Figure 4.8 shows the resistance as a function of displacement for all 6 series.

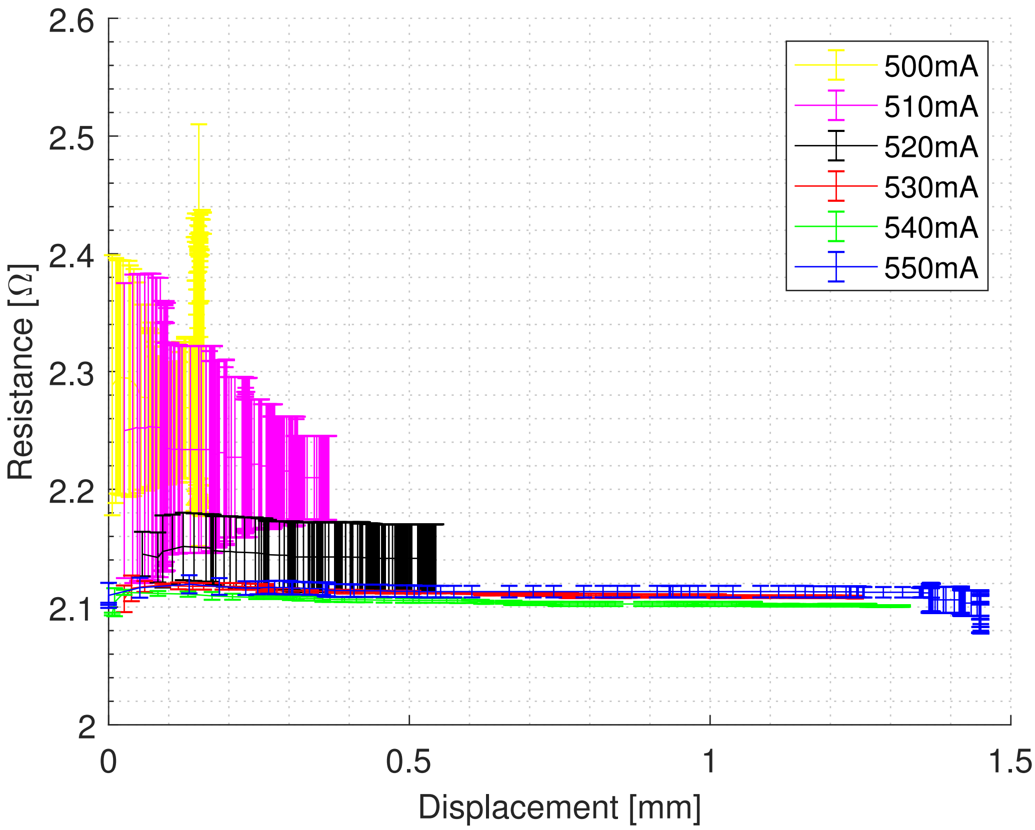

FIGURE 4.8: Resistance as a function of displacement at 500-550 mA input currents

The resistance variation over repeated measurements are large, especially for current settings of $\leq 520\,\mathrm{mA}$, as indicated by the deviation in the same current setting series. Full displacement of $1.45\,\mathrm{mm}$ is also far from being attained at those current levels, as clearly shown in figure 4.8. The variation in the resistance is comparatively smaller for the higher current values $\geq 530\,\mathrm{mA}$. Given the complex and not fully understood mechanics behind the resistance changes in the SMA wire, it is difficult to give an exact answer to the discrepancy seen in the measurements, but there are possible explanations.

The most likely explanation is again due to the PSU. The PSU supplies a constant current, with the voltage being regulated by an internal algorithm that needs time to stabilize. This is further complicated by the complex nature of the SMA wire resistance. The lower currents do not directly induce a phase transition, but there are still internal material changes causing resistance shifts. The PSU attempts to compensate for this full phase martensite resistance change with voltage changes, but the compensation is not accurate enough and either too fast or too slow compared to internal structural changes in the SMA wire responsible for the resistance changes. The basis for this reasoning is simple and can be understood by taking away the low current plots $\leq 520\,\mathrm{mA}$ from figure 4.8, this is shown in figure 4.9, below.

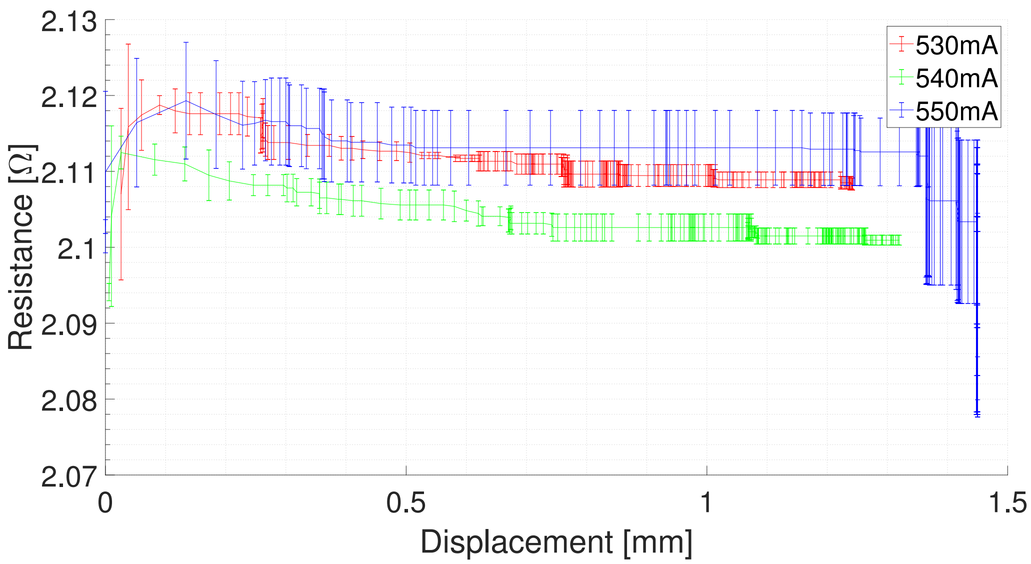

FIGURE 4.9: Resistance as a function of displacement at 530-550 mA input currents

What is clear is that when running appropriate current levels, the previously observed likeness curve of the linear relationship between resistance and strain is apparent, observed by the red and green curves. The problem here the $550\,\mathrm{mA}$ curve, noted in blue. The different result is however explainable. Given that the current level is high enough to induce a phase transformation more rapidly then the for $< 550\,\mathrm{mA}$, the electrical resistance change too quick to be observable with the available means for measurement.

The hypothesis based on the blue curve data does require further testing for confirmation, but this requires a very fine tuning of current supply to the system, of which the current setup is not capable of providing. Hence it not possible to confirm whether this is the case or not. This underlines the need for a different and better suited approach to measure the SMA wire resistance. A way to improve the resistance measurement process is the inclusion of a circuit with appropriate resistance measurement capabilities, which is the next logical step for this project.

4.2 Wheatstone bridge experiment

It is clear from the measurements detailed in Section 4.1 that an optimized resistance measurement method is required. A logical choice for expanding the measurement setup is to include a Wheatstone bridge circuit with one of the elements being the SMA wire.

The main advantage of this type of measurement setup is an inherently more sensitive robust way of measuring the resistance change as opposed to connecting the SMA wire to the PSU directly. In setting up a Wheatstone bridge circuit for measurement additional components and devices are required. A full list of the additional components and devices used are given below in table 4.1.

TABLE 4.1: Additional components and devices for use with the Wheatstone bridge circuit

Producer: Type	**Description**
Unknown: Resistor (x2)	$2.7\,\Omega$(rated) and $10\,\mathrm{k\Omega}$
Unknown: Potentiometer	$10\,\mathrm{k\Omega}$ with 10x360° turn set to $8.3\,\mathrm{k\Omega}$
Analog Devices: AD8203	Difference Amplifier
K and H: Model GL-36	Breadboard
Various lead wires and banana plug connectors	

The first of the design considerations are the Wheatstone bridge resistors. In general the Wheatstone bridge resistor values are of little consequence. It is the ratio of the resistors that determine the overall characteristics. One of the bridge resistors is rated at $2.7\,\Omega$, which is considerably low, given the fact that the resistor itself was picked from storage after an unknown amount of time, it was not possible to be certain of its actual resistance value. It was therefore measured with the best instrument available, a Fluke 179 digital multimeter (DMM) [74]. This fluke has a stated accuracy of $\pm 0.9\% + 2$ on a $600\,\Omega$ range at $0.1\,\Omega$ resolution, with the measured resistance at $7.9\,\Omega$.

This does not constitute a reliable measurement by any accounts. However, it was unfortunately the only component available stated at such low resistance levels and there was no substitute for use. A circuit diagram of the added Wheatstone bridge is included in figure 4.10, and an additional block diagram for an overview of the entire system change in figure 4.11.

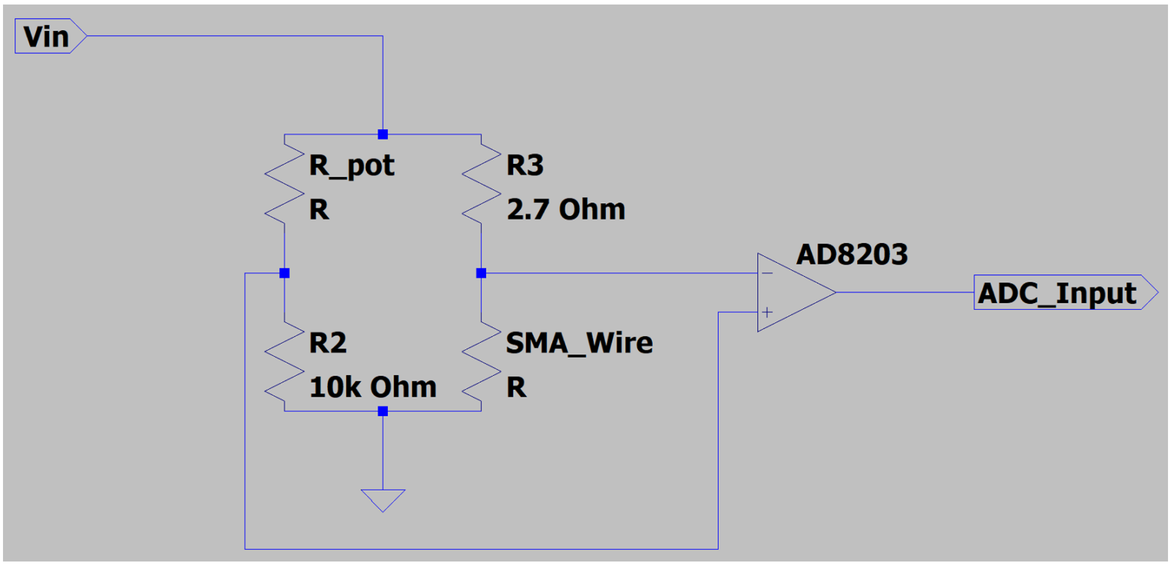

FIGURE 4.10: Wheatstone bridge circuit diagram

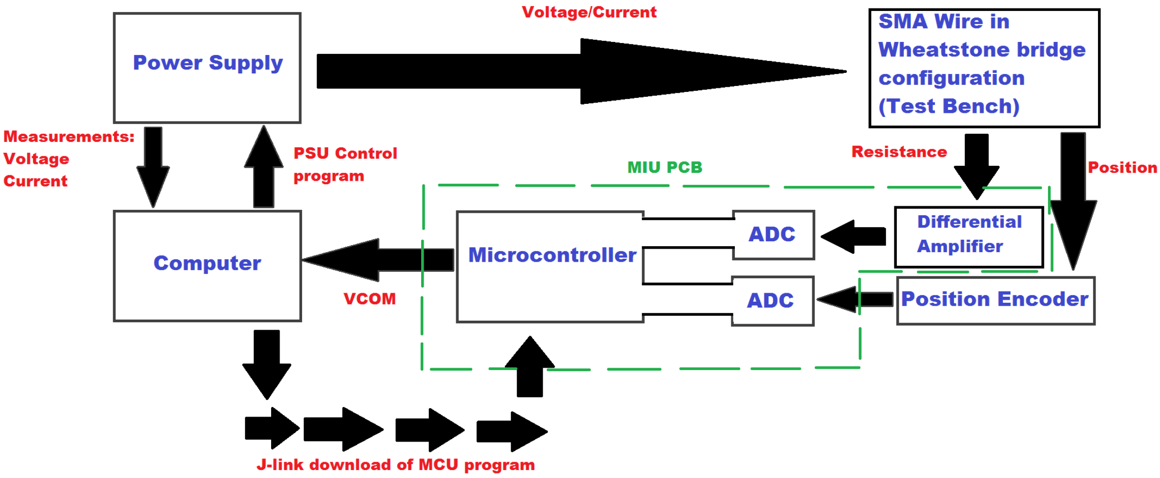

FIGURE 4.11: Block diagram of experiment post modifications

For this specific Wheatstone bridge, one of the bridge resistors are a potentiometer, one is the SMA wire, and the remaining two are regular resistors. This is required since the actual resistance of the SMA wire is not exactly known, nor is initially the circuit supply voltage or current.

Ideally, a Wheatstone bridge circuit can be designed in such a way that the differential voltage values are pre- determined minimum and maximum values. This is done by circuit analysis and Wheatstone bridge equations. For a in depth discussion and illustration of these methods, see [75].

However, for this configuration experimental values have to be made in order to determine the appropriate supply and bridge voltages. The potentiometer is the mediating element capable of regulating between $0\,\Omega - 10\,\mathrm{k}\Omega$. This is useful for balancing the output voltage values of the bridge.

As such, the classic Wheatstone bridge equation for finding the SMA wire resistance has to be altered slightly to account for both supply and output voltages. The full expression is given below

$$R_{SMA} = \frac{R_2 R_3 + R_3(R_{pot} + R_2)\dfrac{V_b}{V_{in}}}{R_{pot} - (R_{pot} + R_2)\dfrac{V_b}{V_{in}}} \tag{4.5}$$

Previously used voltage and current values are only usable as initial reference values, as an increased number of components of the circuit means an overall increase of current and voltage values are to be expected. Additionally, some leaking current across the bridge circuit is expected, and the values of R_pot and R2 are deliberately chosen to be high compared to R3 and the SMA wire. This was in attempt to minimize leaking current in the circuit. When measured with a digital multimeter, the leak current never exceeded $300\,\mu\mathrm{A}$. The leak current is therefore considered negligible.

Furthermore, the Wheatstone bridge output values were measured to a maximum of $\approx 500\,\mathrm{mV}$, at $600\,\mathrm{mA}$ and at full displacement. The bridge output terminals were connected to a differential operational amplifier already located on the MIU board which was used in the previous experiments, as detailed in the block diagram in figure 4.11.

Due to the fact that the MIU board only contains two ADC modules, the temperature sensor had to be disconnected to allow for the processing of the bridge voltage signal. This is an unavoidable consequence of not having additional ADC modules available. The ADC module, as described previously, has an input voltage maximum of $3.3\,\mathrm{V}$. The amplification of the differential operational amplifier, datasheet [76], had to be configured to a suitable level. A circuit schematic of the MIU board amplifier is included in figure 4.12 below.

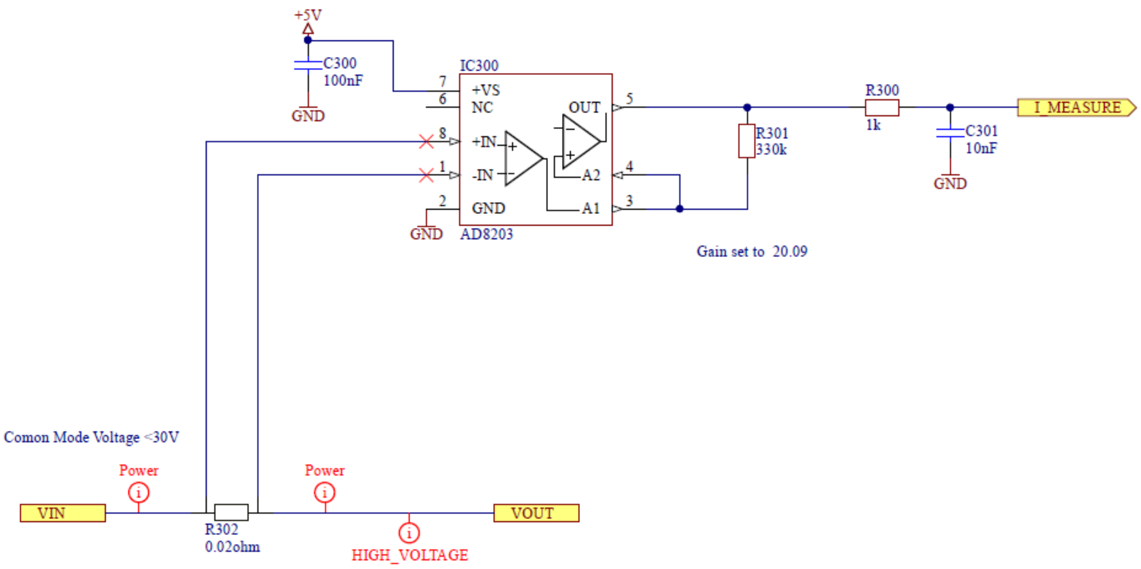

FIGURE 4.12: MIU: Differential operational amplifier circuit schematic

Considering the detailed Wheatstone bridge levels, a reasonable gain for the 3.3 V ADC input would be a gain that puts the input signal to the amplifier a bit below the maximum input. This is to account for potential spikes and general noise. The gain factor calculation was decided to be $G = 500\,\mathrm{mV} * 6 = 3.0\,\mathrm{V}$. Hence, the differential amplifier configuration needed to be reconfigured, as this was pre set to a gain of 20.09, ref figure 4.12. The external resistor and amplifier gain equations are given in the datasheet, reproduced below.

$$G = \frac{14 * R_{external}}{R_{external} + 100k\Omega} \tag{4.6}$$

$$R_{external} = 100k\Omega \frac{G}{14 - G} \tag{4.7}$$

Since the gain factor is known, the equations are easily solved. The MIU board reconfiguration required changing the external resistor to a $75\,\mathrm{k\Omega}$ resistor, given equation 4.7. From the specifications in [76], any gain adjustments to $G < 14$ requires a modification due to the amplifier design.

The AD8203 differential amplifier contains a pre amplifier and a buffer. The pre amplifier has an output resistance of $100\,\mathrm{k\Omega}$. This has to be routed to ground by connecting pins 3 and 4 with an external resistor of value derived above. This meant switching the existing resistor (R301) with the new $75\,\mathrm{k\Omega}$ resistor and rerouting the connection from the output to ground. Furthermore, the R302 resistor on the differential inputs had to be removed because the setup is not designed to measure current, but voltage.

The changes give an effective maximum output of $3.0\,\mathrm{V}$ to the ADC, leaving $300\,\mathrm{mV}$ for general noise and potential spikes. The modifications to the MIU board included soldering of above detailed components. and fixing lead wires to the input pins for the amplifier. It also involved cutting electrical pathways to other parts of the MIU board not in use. This constitutes the expanded experimental setup designed to obtain better resistance measurements of the SMA wire.

However, several issues presented themselves while working on this circuit. The amplifier's output signal was highly erratic, seemingly jumping between any random value in the ADC range. This occured irrespective of current input to the bridge circuit and measurements performed across the circuit terminals. A thorough check of the measurement circuit breadboard, lead wires and connectors followed and a subsequent grounding error was discovered. However, this did not fix the differential amplifier output signal.

Since time and experiment priority was becoming an increasing factor for the remaining time allotted for this project, it was decided to stop any further testing relating to the characterization of the SMA wire and dedicate the remaining time to an equally important aspect, MRI compatibility testing of the miniature motor design.

4.3 MRI compatibility testing: material visibility

Since a proof of concept of an MRI compatible miniature motor was the outline for this project, material and actuator testing within the MRI environment could not be neglected. Regardless of previous material compatibility tests performed on Nitinol [34, 35], individual testing is mandatory due to different manufacturing procedures and potential impurities of the material. Material testing includes bringing the SMA wire samples to an available MRI scanner at Haukeland University Hospital (HUS), to perform pre-defined visibility test sequences. At HUS, NNL has access to a 3 T MRI scanner, model PRISMA by Siemens [77]. This scanner was made available for all subsequent tests relating to this project.

The visibility test are performed relative to a phantom. Industry standard phantoms containing water are employed as they provide optimal signal detection within the clear bounds of the phantom. The visibility test is designed to look for material responses and potential artefact generation relative to the phantom. The SMA material samples are placed on two locations; on the top and the back of the phantom. In addition, a fish oil pill is attached on one side as a reference for a known quality. The idea behind the fish oil pill is simple, the fat content of the pill is similar in response to the fat content of humans, thereby making a fish oil pill a good candidate to visually observe on MRI images, as well as seeing the plastic boundary around the imaging phantom itself. Figures 4.13 and 4.14 show the phantom with the attached SMA wire samples and fish oil pill.

FIGURE 4.13: MRI visibility testing: material placement on phantom - front

Figure 4.13 shows the phantom with the attached fish oil pill on the left and $\approx 90\,\mathrm{cm}$ coiled SMA wire. The top SMA wire sample was coiled specifically because it forms a closed loop which can generate artefacts and affect the visibility test. This was done so on purpose to elicit a worst case in-homogeneity artefact, and compare it to the more reasonable sized SMA wire sample placed on the back of the phantom, as seen in figure 4.14, below.

FIGURE 4.14: MRI visibility testing: material placement on phantom - back

The decision to have both of these samples on the same phantom was intentional, as the material length difference, orientation and geometry is thought to have an effect on the visibility test. The phantom and the wire samples was placed inside a headcoil. The headcoil has internal RF coils acting as receivers. They are located much closer to the examined object, thus providing superior image quality compared to the body coil receivers located around the MRI gantry.

The data processing for these tests were performed with syngo fastview, a Siemens made standalone viewer for MRI images [78]. Since MRI is primarily used as a diagnostic tool, the image sequences from the tests come in anatomically defined cross sectional planes. These plane orientations are defined as sagittal, coronal and transverse, illustrated here [79]. The planar orientation for subsequent visibility testing are shown relative to figure 4.13 below in figure 4.15.

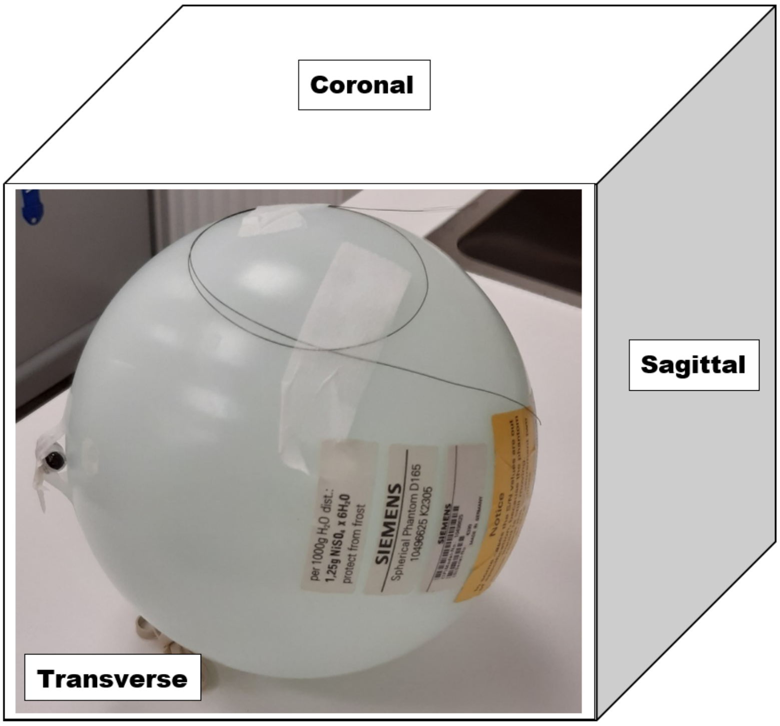

FIGURE 4.15: Planar cross sectional orientation on phantom

The sagittal plane images are scanned left to right, being first exposed to the fish oil pill. Similarly, the transverse plane images scan starts at the front, approximately where the Siemens labels are located, and ends at the sampled SMA wire used for experiments. Lastly, the coronal plane image scan starts at the bottom and ends up at the coiled SMA wire sample.

A total of three visibility tests were performed, along the respective planes previously mentioned. Each of the three sequences has a total of 30 images. Due to the volume of images and the post processing impact on observable effects, i.e. brightness and contrast settings have a huge impact on observable information on a single image, only a few select images with the most highlighted and clearly visible information are presented.

FIGURE 4.16: Visibility testing: sagittal plane

The dark spots on the left side on the image is the signal blockage from the SMA wire loop from a sagittal plane orientation view. The signal blockage is clearly visible and appear as a slightly faint circle, corresponding to the SMA wire loop. Figure 4.17 below, shows the transverse plane visibility test.

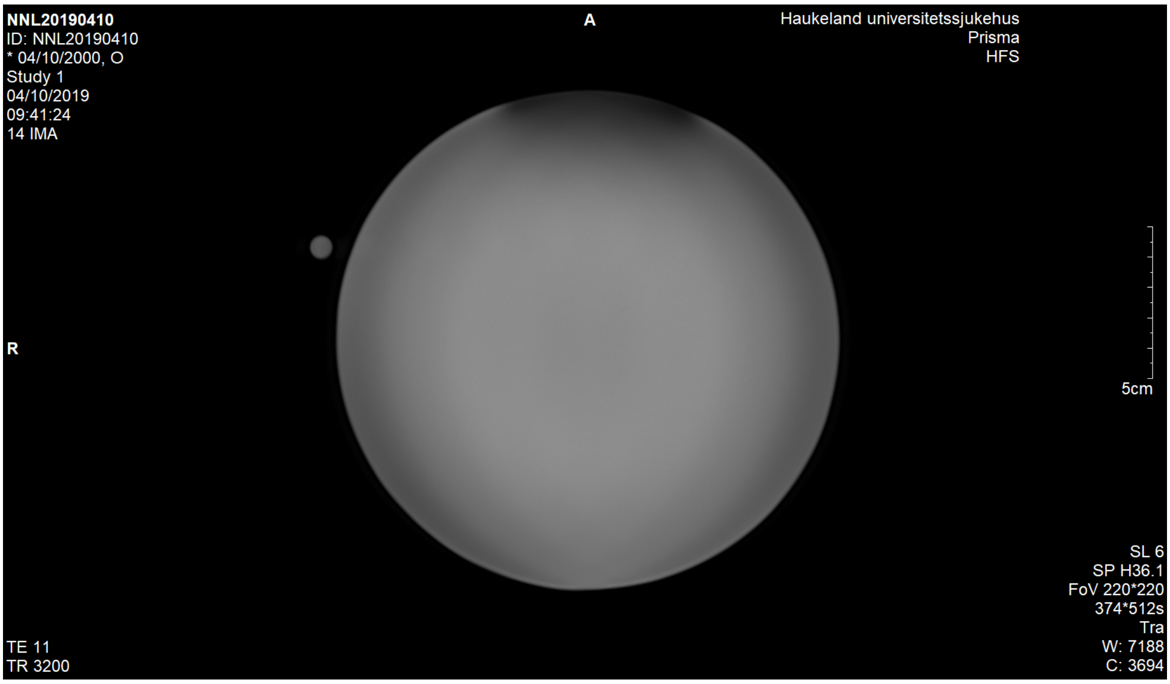

FIGURE 4.17: Visibility testing: transverse plans

This shows a different angle of the artefact generated by the coiled SMA wire, as well as providing a contrast by showing the signal detected in the fish oil pill attached on the side. Lastly, the coronal planar test result, shown in figure 4.18 below.

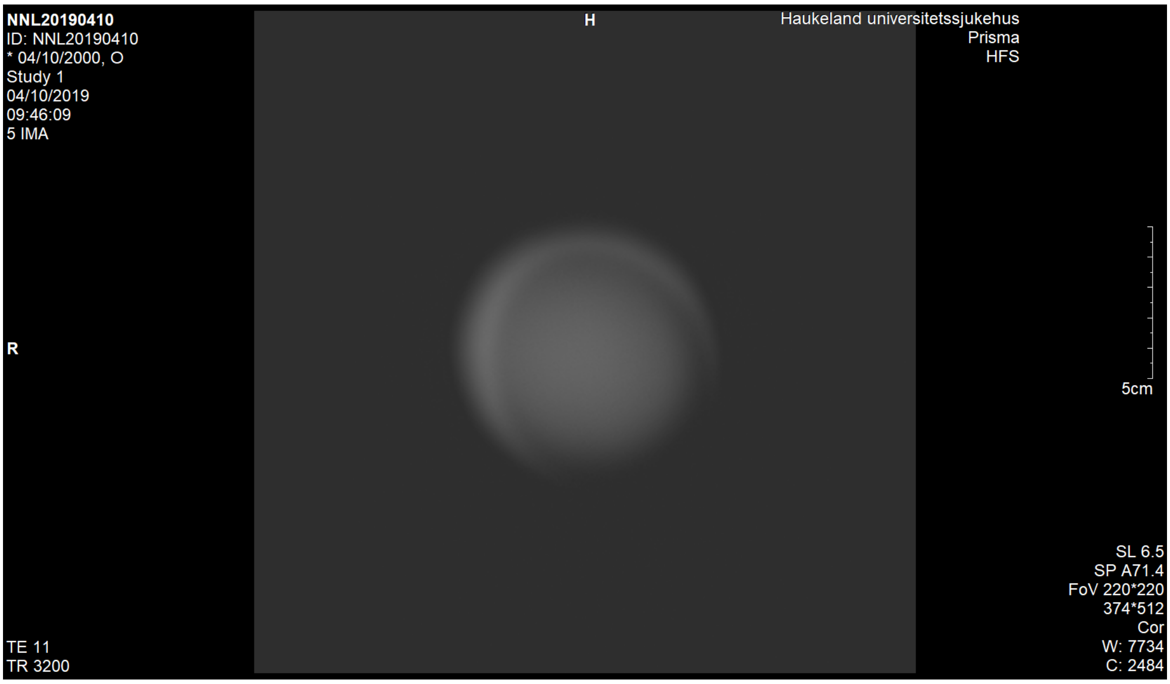

FIGURE 4.18: Visibility testing: coronal plane

The shaded circular region that overlays the lighter grey is the artefact generated by the coiled SMA wire, seen above from different angles. It is evident from the presented images that there is no signal detection in either SMA wire samples. This is based on the clear signal detection example provided by the fish oil pill, seen in figure 4.17. There is a degree of artefact generation in the form of a signal void area that appears as a dark or black spot. The areas where this artefact is observed is consistent with the coiled SMA wire sample, located on the top of the phantom as seen in figure 4.13.

No visibility or artefacts were observed on any of the tests for the attached SMA wire on the back of the phantom, figure 4.14. It is speculated that the SMA wire either is too small for detection when uncoiled and/or that the orientation of the sample minimize the potential for artefacts. Moreover, artefacts related to the small SMA wire is not neglected, as it is likely to produce some artefacts if connected to a power source with a running current. However, the initial results are promising in that smaller lengths of SMA wire are unlikely to cause large artefacts. Considering external device integration, the realistic placement scenario for the SMA wire material would be outside the imaging region in an RF shielded housing. In conclusion, the visibility tests provided promising observations to support that fact, but further testing is required to completely assess the SMA wire material.

4.4 MRI immunity testing

The next step in the MR testing required bringing the test bench to the MRI scanner at HUS. This meant the test bench had to be screened for any magnetic responses. Prior to this however, it was decided to forego most of the measuring capabilities the previous tests had employed. The reasons for this were several, with the main reason being the position encoder being inherently magnetic and could not be used inside the MRI environment. Furthermore, new lead wires had to made since the wire length required for connecting the test bench inside the MRI scanner to the outside of the room were $\approx 8\,\mathrm{m}$ long. This constituted non-negligible signal losses difficult to predict and account for and would have required adjustments in the measurement circuitry.

Moreover, availability of the MRI facilities and time constraints were also a large factor. It would not have been enough time to make appropriate adjustments to the MIU board, the breadboard measurement circuitry and the test bench in the short time frame prior to the allotted time at the MRI facilities at HUS. Lastly, the considered state of the system characterization. No definitive control system has been developed due to the need for more complex circuitry, instrumentation and testing. Since neither a control system or an MR compatible position encoder is available at this time, the testing options are limited.

The goal of the test was decided to simply document the SMA wire actuation when placed in the MRI gantry, both during a passive and active state of the MRI scanner. This is essentially referred to as an immunity test, as noted by co-supervisor Stian Sagevik. Immunity test means simply confirming whether or not the device is capable of operating in an MRI environment without apparent adverse effects.

4.4.1 Reconfiguring the test bench

The test bench itself was made of aluminum and was initially considered as MR safe. Nevertheless, all elements went through a separate test at NNL prior to bringing the test bench to the MRI facilities at HUS. This testing was done with a strong $1\,\mathrm{T}$ magnet block at the NNL laboratory. All the screws in the test bench tested as magnetically attractive and had to be replaced. Replacement non magnetic screws were found at the NNL laboratory. Additionally, the axle and wheel on which the position encoder and weight hanged off of was also magnetic and had to be replaced.

Unfortunately, no replacement metal axle with plastic wheel could be obtained in a short time frame, and a replacement tooth pick was used instead. The position encoder and the thermistor were also removed from the test bench. The weight is made of brass and does therefore not pose a risk in a magnetic field. The connector between the SMA wire and the wire holding the brass weight also needed to be replaced. Fortunately, a previously 3D printed nylon connector was refitted to replace the connector.

The 3D printed nylon connector was originally intended for use with the test bench due to its non magnetic properties. However, it was discarded due to difficulties in fastening the SMA wire during actuation. The plexiglass cover to limit airflow was used as a stand during the tests. This was necessary due to having the test bench elevated to accommodate the free hanging weight and airflow containment was not an objective for testing. A point of concern was how to document the phase transformation of the SMA wire without a position encoder or control system. A basic, but effective, way to observe this transformation was to attach two pieces of folded paper taped in black to the toothpick in a cross configuration, seen in figure 4.19.

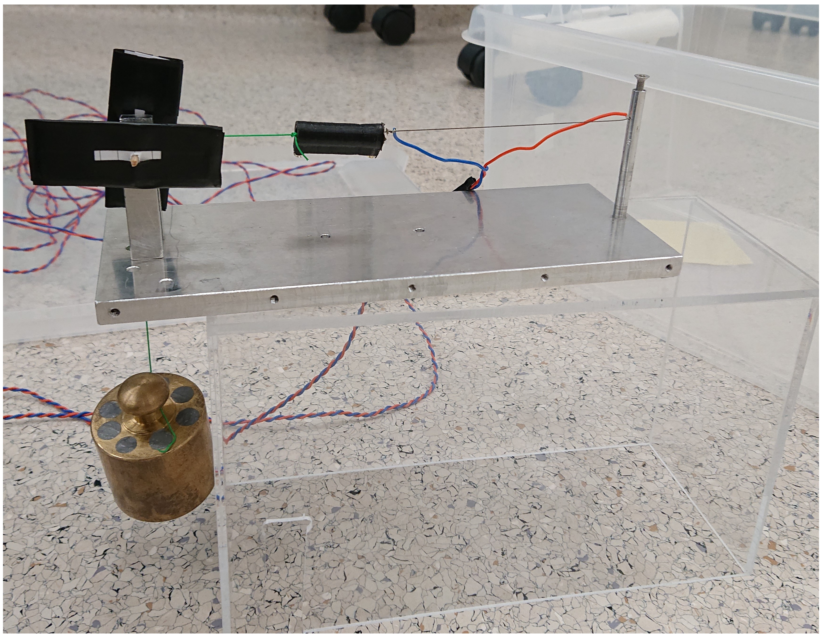

FIGURE 4.19: MRI compatibility testing: reconfigured test bench prior to MRI scanner placement

The modified test bench as described above with the unnecessary parts removed, refitted non-magnetic screws and the taped paper folds to observe the SMA wire contraction. This could easily be turned in such a way as to set an initial position before heating the SMA wire, and observe the rotation of the paper folds during heating and cooling. It was theorized that any potential effects on the heating and cooling process would either, speed up, slow down or in some other unforeseen way change the behavior of the SMA wire while powered.

4.4.2 SMA motor testing

Figure 4.20 below shows the test bench placed inside the MRI gantry. The objects behind the test bench is a phantom object, as without this phantom the scanner would not be able to run. The test bench was placed close to the phantom to allow the gradient field and RF effects to have as much an effect as possible while running an imaging sequence.

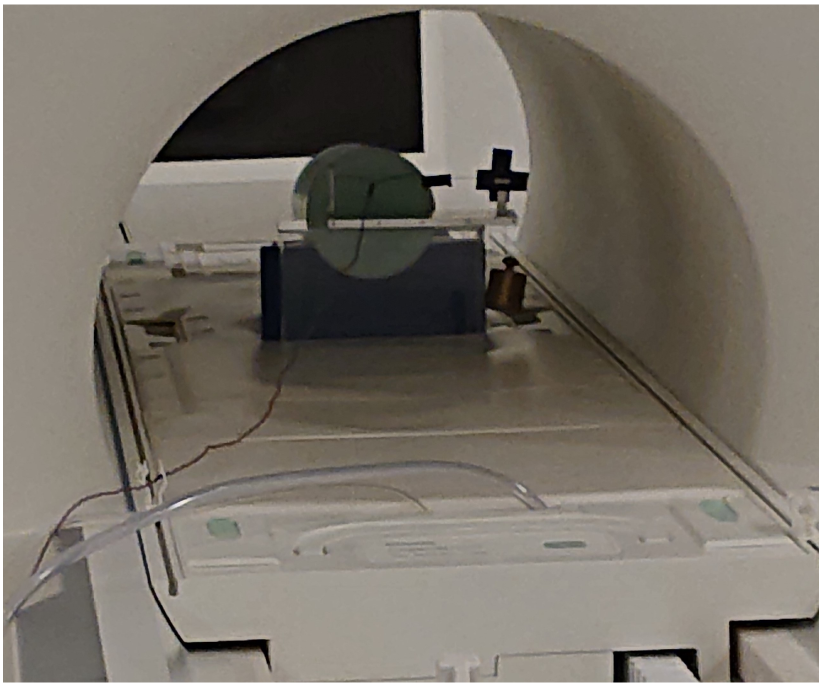

FIGURE 4.20: MRI compatibility testing: reconfigured test bench placed inside MRI scanner

No cameras with high-end optical zoom were available. A smart phone with 6x optical zoom was used to take the pictures. Taking the pictures required the camera to be at the far end of the MRI scanner, since moving closer to the MRI scanner would shut the smart phone display off and potentially damage the circuitry. The power cable seen on figure 4.20 is connected to the PSU being controlled from a computer outside the MRI room. This is shown in figure 4.21, with the hole in the wall being a connection point for wires from outside to inside the MRI scanner room.

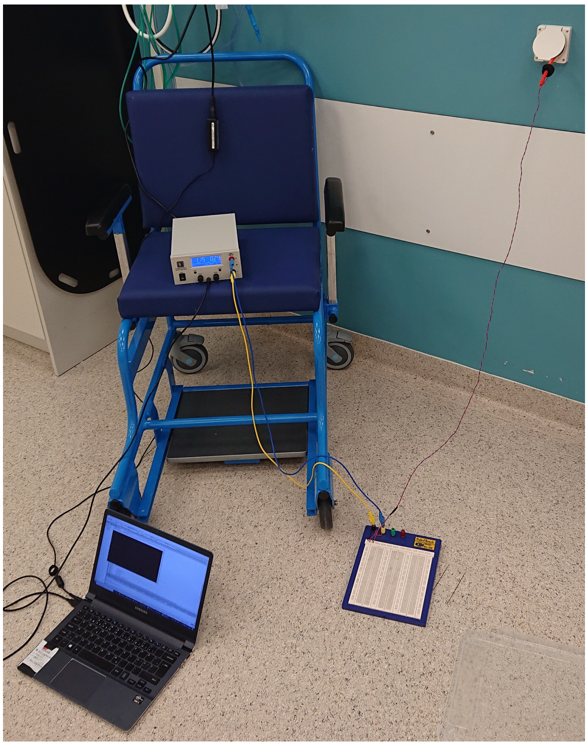

FIGURE 4.21: MRI compatibility testing: computer controlled PSU outside MRI scanner room

The banana plugs connectors used on the PSU was connected in the easiest way available, via the existing breadboard. This configuration setup was tested beforehand, with preset settings consisting of 2 steps. First, a 60 seconds low power mode of $300\,\mathrm{mA}$ CC mode with $\approx 1.0\,\mathrm{V}$ designed to work as a baseline for an initial setting not inducing any phase transformation of the SMA wire. Second, a 60 seconds high power mode of $650\,\mathrm{mA}$ CC mode with $\approx 2.0\,\mathrm{V}$ designed to work as a step, inducing a large degree of phase transformation resulting in maximum contraction of the SMA wire.

The maximum current was set conservatively, as opposed to the passive cooling tests at $900\,\mathrm{mA}$, due to some safety concerns at higher levels of effect. The safety concerns specifically relate to resonance effects and heat build up in lead wire ends on both sides of the setup. Calculating the effective resonance length requires experimentally determined relative permittivities for any given conductor. This is beyond the scope of this project, and a simplified quantitative based calculation sufficed.

The resonance wavelength relationship is given by $c = \lambda f \sqrt{\epsilon_r}$, solved for λ. However, a rough estimate value is sufficient since it is a decreasing factor for the effective resonance length. The lead wires connecting the SMA wire to the PSU are several times longer, $\approx 8\,\mathrm{m}$, than the resonance length for free space, see [80] for table reference values. For estimation based on a Siemens 3T Prisma MRI scanner with $\omega_L \approx 127.74\,\mathrm{MHz}$ and the permittivity of free space, this equals a resonance length of $\approx 1.2\,\mathrm{m} \pm 0.2\,\mathrm{m}$, given some leeway due to the rough estimation. Resonance harmonics fall approximately at n-multiples of the resonance length. This equates to $\approx 7.2\,\mathrm{m} \pm 0.2\,\mathrm{m}$ at $n = 6$ and $\approx 8.4\,\mathrm{m} \pm 0.2\,\mathrm{m}$ at $n = 7$. It is however difficult to base a risk assessment on these rough figures, and it was brought to the attention of Hardware Developer Svein Reidar Rasmussen at NNL, and given the go to proceed after careful consideration based on years of experience doing extensive testing on external electronic equipment in MRI environments.

For testing inside the MRI scanner, two separate tests were performed. First, where the MRI scanner was not running an imaging sequence, and second, when the MRI scanner was in operation. For the first test run with the MRI scanner in non-operation mode, the sequence performed with no complications for the duration of the test. No visible changes was observed on the lead wires and no induced heating was noticed on the outside of the MRI scanner room. Checks for heat induction on the connectors was done by Hardware Developer Svein Reidar Rasmussen. The phase transformation was observed from inside the MRI scanner room, with the paper folds visibly rotating $\approx 90^\circ$ at the onset of the high power sequence, and returning to initial position upon sequence shut down.

For the second test, with the MRI scanner in operation, two separate sequences were performed. Both sequences are Siemens defined standardized sequence tests with T1 and T2 image weight, respectively. For a primer on differences in imaging sequence techniques, see [11] chapters 2, 3 and 4. Observations were made with no complications for the duration of both tests. No heating occured on or near the connectors as checked by touch, and no adverse effects were observed from inside the scanner room for the entirety of the two sequences. The paper folds rotated again by $\approx 90^\circ$, same as when the MRI scanner was not in operation. One interesting effect on the lead wires that took place when testing was when the high power sequence started. The lead wires visibly suspended parallell to the static magnetic field, due to the mutual interaction by the static magnetic field of the MRI and the induced magnetic field resulting from the current. This was however only observed for the high powered part of the tests, at $650\,\mathrm{mA}$ and $\approx 2\,\mathrm{V}$, and not the low powered part at $300\,\mathrm{mA}$ and $\approx 1.0\,\mathrm{V}$.

Moreover, the paper fold rotation while testing at the MRI facilities was, as mentioned above, $\approx 90^\circ$ during all tests in the MRI gantry. However, when performing pre-tests, at the laboratory in the NNL offices, on the setup to determine the optimal current settings, the observed paper fold rotations were consistently $\approx 180^\circ$. This $\approx 90^\circ$ difference is attributed to eddy currents in the brass weight when it is being pulled upwards during the contraction of the SMA wire. The eddy currents induced in the brass weight are opposite to the relative direction in the magnetic field exerting a force that pulls the weight in the opposite direction. This resulted in an effective resistance to the contraction and elongation during phase transformation, effectively limiting the rotation and possibly the recovery strain of the SMA wire.

Overall, the modified test bench tests at the MRI facilities at HUS are considered a success. It was shown that the SMA wire is able to be actuated while the MRI scanner is in operation, serving to verify the immunity test was a success. Interestingly, the resonance length concern was unwarranted. No significant heating of the connectors were observed during any of the tests. There is a possibility this could perhaps be due to a relatively standard RF intensive test, or even that the resonance length alteration by physically touching the connectors attributed to significant heat loss.

Another concern was that the motor would potentially be unable to hold a static position while inside the MRI scanner. The reason for this is the current loop effectively formed by the system setup. Since it will induce magnetic effects opposing the current flow, observing oscillations in the actuation was considered a possibility. It is unfortunately inconclusive whether or not this is a fact, since no definite quantified numbers were obtainable during the testing at the MRI facilities. The basic confirmation of the functionality of the SMA motor actively running during an MRI scan has been confirmed. Any further testing requires added instrumentation, functionality on the measurement setup and preferably a working control system. Lastly, a different method for placing the SMA wire under constant stress is desirable, to circumvent the effects observed on the brass weight leading to reduced displacement range(s).

Chapter 5

Summary and Conclusion

MRI compatible miniature motors represent a multi-discipline branching challenge. One that requires knowledge of underlying and surrounding physics, with theoretical and practical aspects being equally complex. The logic behind beginning to tackle this challenge started with research, to acquire a greater understanding of MRI technology and magnetism in general. This provided the starting point for the project, while also providing a solid foundation upon which to base design choices and direction related to furthering the project goals. Once this was established, a proper consideration of existing technologies and research were made. This consideration process consisted of several factors; simplicity, size, power requirements, safety, academic interest and cost. All of which helped determine which path to pursue.

SMA miniature motors as a whole are still a relatively recent technology. As such, many aspects of the material characterization performed in research is subject to changes depending on differences in manufacturing processes. This meant that any design process needed to start at a fundamental level. Initially it was presumed that this phase would be less time consuming, and require less insight and work with all elementary parts of the experimental setup. Thus, giving more time to map, plan, test and determine viability of various control system designs for the miniature motor. Evidently, this was not the case. Deciding and designing the test setup, components, measurement circuits, finding relevant instruments and employing previously unknown microcontrollers with unfamiliar architecture consumed a lot of time. It meant learning new software tools and several non-trivial aspects of embedded programming.

Additionally, with every system comes the possibility of complications. This project was no exception to that fact. Along the way of designing and setting up the test setup for data processing and measurements came several technical problems. Mostly, these problems were related to either a lack of understanding of embedded programming and/or general electronics issues. Many of the problems would have taken a lot more time to fix had it not been for the assistance of co-supervisor Olav Birkeland. Nevertheless, a basic test design with limited functionality for measurements were developed and shown to be working within expected margins. Furthermore, basic control interface and logging of measurement data have all been designed and represent a good foundation for further work.

The last technical problems encountered relating to the differential amplifier were not solved. The proposed solution was to test with a different differential amplifier to see if it was a case of a faulty IC. However, with time constraints it was felt appropriate to proceed with another key aspect of this project, MRI compatibility. The materials and a reconfigured test bench was brought to the MRI facilities at HUS where testing was performed. The allotted time window for testing was limited, and as a result, follow up testing was not available for the remaining project time.

The MRI compatibility tests did however perform well. The tests represent the culmination of combined theoretical and practical study, and serve as an initial confirmation of proof of concept for the use of SMA wire actuation based motors as viable for use in MRI environments. Many aspects of the whole system still require a lot more work before it can be considered viable for any sort of implementation with existing NNL systems. As it stands, the ground work has been laid and the system is capable of and ready to be taken to the next stage of development.

Chapter 6

Future Work

Many important aspects for the realization of this project as more than a proof of concept remain. The first of which is to continue the mapping of the motor characteristics and to develop a working control system. As stated several times, the most straightforward way of achieving this is to continue to explore the relationship between the strain and the resistance, or in this project's case the displacement and the resistance.

Ideally, it is preferable to purchase more accurate, and expensive, position encoder for a full mapping of the expected strain range, as opposed to the limited range of the position encoder used in this project. The same thing applies for a better suited power supply. In that regard, an optimized circuit with possible MOSFETs working as current supply for the SMA would be a cheaper, and better suited for this purpose. Furthermore, another requirement includes introducing a different differential amplifier. That is, if the proposed Wheatstone bridge is to be further employed. If this is chosen, the existing measurement data can in all probability work as a rough baseline comparison for further mapping purposes, given that similar parameters are used for testing.

Alternatively, considering the reported discrepancies between the low resistivity and the initial obtained resistance measurements. If the Wheatstone bridge does not provide sensitive enough results, a modification to the measurement approach could be to use a Kelvin bridge design, or a Kelvin ohmmeter [81]. This would in all probability be preferable to a Wheatstone bridge because it would essentially take away the parasitic resistance elements of the lead wires and connectors in the circuit, leading to optimal conditions for low resistance measurements. This is, by all means, a challenge in itself to set up and test, but could potentially be a good solution.

For the specific purpose of integration with NNL's VSHD goggle system as an automatic lens focusing controller with a maximum displacement range of $1.0\,\mathrm{mm}$, lowest possible power requirements and the small housing area available. A short SMA wire is needed. For an SMA wire of $4.0\,\mathrm{cm}$, a $1.0\,\mathrm{mm}$ displacement range utilizes a little more than half (2.5%) of the reported recovery strain range of $\approx 4\,\%$. Based on the experiences gained through this project, it is estimated that to actuate such a SMA wire to $1.0\,\mathrm{mm}$ displacement in a significantly confined space would at most require $\approx 1.0\,\mathrm{W}$ for a rapid transformation, and significantly lower to maintain the position. However, the time required for a full sized imaging sequence may pose associated heating risks for any connectors and the housing. Additionally, the time required for the SMA wire to return to its original length will be considerable solely due to the confined space.

As such, one possible solution would be to configure the SMA wire to adjust the lens in steps, thereby powering the SMA wire in pulses. This could be done by attaching the SMA wire to a small cogwheel with a step wise lockable position that resets upon a full $360°$ revolution, implied in this is a one way position control. The constant stress requirement for the SMA wire could be implemented by attaching a plastic spring. Since the displacement range is small there should be little cause for concern regarding a change in the spring constant, and by using plastic the spring's coil configuration is a non-issue for the magnetic environment.

References

[1] G.A. Krieger, R. Fichtinger, E. Atalar, and L. Whitcomb. “Design of a novel MRI compatible manipulator for image guided prostate intervention”. In: (2004).

[2] B.T. Larson, A.G. Erdman, N.V Tsekos, E. Yacoub, P. Tsekos, and I.G. Koutlas. “Design of an MRI-compatible robotic stereotactic device for minimally invasive interventions in the breast”. In: *Journal of Biomechanical Engineering* (2004).

[3] K. Masamune, E. Kobayashi, Y. Masutani, M. Suzuki, T. Dohi, H. Iseki, and K. Takakura. “Development of an MRI-compatible needle insertion manipulator for stereotactic neurosurgery”. In: *Journal of Image Guided Surgery: Official Journal of the International Society for Computer Aided Surgery (ISCAS)* (1995).

[4] N. Hata, F. Ohara, R. Hashimoto, M. Hashizume, and T. Dohi. “Needle guiding robot with five-bar linkage for MR-guided thermotherapy of liver tumor”. In: (2004).

[5] H. Elhawary, A. Zivanovic, M. Rea, B.L. Davies, C. Besant, D. McRobbie, N.M. Desouza, I. Young, and M.U. Lamperth. “A modular approach to MRI-compatible robotics”. In: *IEEE Engineering in medicine and biology magazine* (2008).

[6] K. Uchino. “Piezoelectric ultrasonic motors: overview”. In: *Smart materials and structures* (1998).

[7] J. Mcmahon. *11 ways piezoelectric motors improve equipment performance*. 2010. URL: https://www.controleng.com/articles/11-ways-piezoelectric-motors-improve-equipment-performance/.

[8] P.E. Watson, I.D. Watson, and R.D. Batt. *Total body water volumes for adult males and females estimated from simple anthropometric measurements*. 1980. URL: http://dx.doi.org/10.1093/ajcn/33.1.27.

[9] J.M.D. Coey. *Magnetism and Magnetic Materials*. Cambridge University Press, 2010.

[10] H.D. Young and R.A. Freedman. *Sears and Zemansky's University Physics with Modern Physics*. 13th ed. Pearson, 2014. ISBN: 978-1-292-02063-1.

[11] M.T. Vlaardingerbroek and J.A. den Boer. *Magnetic Resonance Imaging: Theory and Practice*. 3rd ed. Springer, 2004.

[12] A.D. Elster. *Brands of MRIs*. URL: `http://mriquestions.com/brands-of-scanners.html`.

[13] *Courtesy of Allen D.Elster*. Accessed: 2019-07. URL: `http://www.MRIquestions.com`.

[14] L.P. Panych and B. Madore. "The physics of MRI safety". In: *Journal of Magnetic Resonance Imaging* (2018).

[15] Expert Panel on MR Safety: E. Kanal, A.J. Barkovich, C. Bell, J.P. Borgstede, W.G. Bradley Jr, J.W. Froelich, J.D. Gimbel, J.W. Gosbee, E. Kuhni-Kaminski, et al. "ACR guidance document on MR safe practices: 2013". In: *Journal of Magnetic Resonance Imaging* (2013).

[16] R. Turner. "Gradient coil design: a review of methods". In: *Magnetic resonance imaging* (1993).

[17] Geek3. *File:VFPt anti-helmholtz coil thumb1.svg*. Accessed: 2019-06. 2013. URL: `https://commons.wikimedia.org/wiki/File:VFPt_anti-helmholtz_coil_thumb1.svg`.

[18] F. Schmitt. "The Gradient System . Understanding Gradients from an EM Perspective : (Gradient Linearity , Eddy Currents , Maxwell Terms Peripheral Nerve Stimulation)". In: 2013.

[19] A.D. Elster. *Gradient heating*. URL: `http://mriquestions.com/gradient-heating.html`.

[20] P. Keller. *Technologies for Precision Magnetic Field Mapping*. Accessed: 2019-06. 2015. URL: `https://www.metrolab.com/wp-content/uploads/2015/07/General_tech_note_Technologies_for_Precision_Magnetic_Field_Mapping.pdf`.

[21] *Spherical Coordinates*. Accessed: 2019-04. URL: `https://www.mathworld.wolfram.com/SphericalCoordinates.html`.

[22] C.N. Chen and D.I. Hoult. *Biomedical magnetic resonance technology*. Bristol ; New York : A. Hilger, 1989. ISBN: 0852741189.

[23] M. Abramowitz and I.A. Stegun. *Handbook of Mathematical Functions with Formulas, Graphs, and Mathematical Tables*. Dover, 1964.

[24] M. Wendt. *Second Order Shimming of High Magnetic Fields*. URL: `https://www.healthcare.siemens.com/siemens_hwem-hwem_ssxa_websites-context-root/wcm/idc/groups/public/@global/@imaging/@mri/documents/download/mdaw/mtqy/~edisp/second_hot_topic_brochure-00017029.pdf`.

[25] *Magnetom Prisma*. Accessed: 2019-06. URL: https://www.healthcare.siemens.com/magnetic-resonance-imaging/3t-mri-scanner/magnetom-prisma/technical-details.

[26] *SIGNA^{TM} Premier – 70cm*. Accessed: 2019-06. URL: https://www.gehealthcare.com/en/products/magnetic-resonance-imaging/3-0t/signa-premier.

[27] M.F. Dempsey, B. Condon, and D.M. Hadley. "Investigation of the factors responsible for burns during MRI". In: *Journal of Magnetic Resonance Imaging: An Official Journal of the International Society for Magnetic Resonance in Medicine* (2001).

[28] J.F. Schenck. "Safety of strong, static magnetic fields". In: *Journal of magnetic resonance imaging* (2000).

[29] C.A. Balanis. *Antenna Theory: A Review*. 1992. URL: https://ieeexplore.ieee.org/document/119564/authors#authors.

[30] J. Pictet, R. Meuli, S. Wicky van Doyer, and J. J van der Klink. "Radiofrequency heating effects around resonant lengths of wire in MRI". In: *Physics in medicine and biology* (2002). DOI: 10.1088/0031-9155/47/16/312.

[31] W.R. Nitz, A. Oppelt, W. Renz, C. Manke, M. Lenhart, and J. Link. "On the heating of linear conductive structures as guide wires and catheters in interventional MRI". In: *Journal of Magnetic Resonance Imaging* (2001). URL: https://onlinelibrary.wiley.com/doi/abs/10.1002/1522-2586%28200101%2913%3A1%3C105%3A%3AAID-JMRI1016%3E3.0.CO%3B2-0.

[32] E.K. Keeler, F.X. Casey, H. Engels, E. Lauder, C.A. Pirto, T. Reisker, J. Rogers, D.J. Schaefer, and T. Tynes. "Accessory equipment considerations with respect to MRI compatibility". In: *Journal of Magnetic Resonance Imaging* (1998).

[33] John F. Schenck. "The role of magnetic susceptibility in magnetic resonance imaging: MRI magnetic compatibility of the first and second kinds". In: *Medical Physics* (). accessed: 2019-01-16. URL: https://aapm.onlinelibrary.wiley.com/doi/abs/10.1118/1.597854.

[34] A. Melzer, St. Michitsch, S. Konak, G. Schaefers, and T.H. Bertsch. "Nitinol in Magnetic Resonance Imaging". In: *Minimally Invasive Therapy & Allied Technologies* (2004). URL: https://doi.org/10.1080/13645700410020269.

[35] M. Ho and J.P. Desai. "Towards a MRI-compatible meso-scale SMA-actuated robot using PWM control". In: 2010. DOI: 10.1109/BIOROB.2010.5626044.

[36] A. Bjørnerud. *The Physics of Magnetic Resonance Imaging FYS-KJM 4740*. Accessed: 2019-06-18. University of Oslo, Department of Physics, 2008.

[37] *Images provided by Hardware Developer Svein Reidar Rasmussen and EVP Engineering Co-supervisor Stian Sagevik*.

[38] R. Gassert, A. Yamamoto, D. Chapuis, L. Dovat, H. Bleuler, and E. Burdet. "Actuation methods for applications in MR environments". In: *Concepts in Magnetic Resonance Part B: Magnetic Resonance Engineering: An Educational Journal* (2006).

[39] N.B. Yu and R. Riener. "Review on MR-compatible robotic systems". In: IEEE. 2006.

[40] *Magnetom Prisma*. URL: https://www.healthcare.siemens.com/magnetic-resonance-imaging/3t-mri-scanner/magnetom-prisma/technical-details.

[41] D.J. Bell, T.J. Lu, N.A. Fleck, and S.M. Spearing. "MEMS actuators and sensors: observations on their performance and selection for purpose". In: *Journal of Micromechanics and Microengineering* (2005).

[42] G.S. Fischer, I. Iordachita, C. Csoma, J. Tokuda, S.P. DiMaio, C.M. Tempany, N. Hata, and G. Fichtinger. "MRI-compatible pneumatic robot for transperineal prostate needle placement". In: *IEEE/ASME transactions on mechatronics* (2008).

[43] H. Zhao, X. Liu, H.M. Zaid, D.J. Shah, M.J. Heffernan, A.T. Becker, and N.V. Tsekos. *Early studies of a transmission mechanism for MR-guided interventions*. 2018. URL: https://scholars.houstonmethodist.org/en/publications/early-studies-of-a-transmission-mechanism-for-mrguided-interventions(69386141-6523-4c8a-aec2-1fac72ae1453).html.

[44] K. Hynynen, A. Darkazanli, E. Unger, and J.F. Schenck. "MRI-guided noninvasive ultrasound surgery". In: *Medical physics* (1993).

[45] K. Masamune, E. Kobayashi, Y. Masutani, M. Suzuki, T. Dohi, H. Iseki, and K. Takakura. "Development of an MRI-compatible needle insertion manipulator for stereotactic neurosurgery". In: *Journal of Image Guided Surgery: Official Journal of the International Society for Computer Aided Surgery (ISCAS)* (1995).

[46] Y. Wang, G.A. Cole, H S.U, J.G. Pilitsis, and G.S. Fischer. "MRI compatibility evaluation of a piezoelectric actuator system for a neural interventional robot". In: (2009).

[47] H. Su, D.C. Cardona, W.J. Shang, A. Camilo, G.A. Cole, D.C. Rucker, R.J. Webster, and G.S. Fischer. "A MRI-guided concentric tube continuum robot with piezoelectric actuation: a feasibility study". In: (2012).

[48] K. Spanner and B. Koc. "Piezoelectric motors, an overview". In: *Actuators*. 2016.

[49] E. Richer and Y. Hurmuzlu. "A high performance pneumatic force actuator system: Part I—Nonlinear mathematical model". In: *Journal of dynamic systems, measurement, and control* (2000).

[50] B. Yang, U.X. Tan, A.B. McMillan, R. Gullapalli, and J.P. Desai. "Design and control of a 1-DOF MRI-compatible pneumatically actuated robot with long transmission lines". In: *IEEE/ASME transactions on mechatronics* (2011).

[51] G. Ganesh, R. Gassert, E. Burdet, and H. Bleuler. "Dynamics and control of an MRI compatible master-slave system with hydrostatic transmission". In: *Robotics and Automation, 2004. Proceedings. ICRA'04. 2004 IEEE International Conference on*. IEEE. 2004.

[52] E. Wilhelm, C. Richter, and B.E. Rapp. "Phase change materials in microactuators: basics, applications and perspectives". In: *Sensors and Actuators A: Physical* (2018).

[53] S. Ogden, L. Klintberg, G. Thornell, K. Hjort, and R. Bodén. "Review on miniaturized paraffin phase change actuators, valves, and pumps". In: *Microfluidics and nanofluidics* (2014).

[54] G. Lupi, A. Scorza, M.L. Rugiano, S.A. Sciuto, and F. Bini. "Preliminary study for a water-paraffin based phantom in MRI quality assurance test". In: *Medical Measurements and Applications (MeMeA), 2015 IEEE International Symposium on*. IEEE. 2015.

[55] K. Ikuta. "Micro/miniature shape memory alloy actuator". In: *Robotics and Automation, 1990. Proceedings., 1990 IEEE International Conference on*. IEEE. 1990.

[56] K. Ikuta, M. Tsukamoto, and S. Hirose. "Shape memory alloy servo actuator system with electric resistance feedback and application for active endoscope". In: (1988).

[57] C. Hiroki, Y. Takaei, Y. TAKEDA, A. SUZUKI, and T. SAKUMA. "Exploitation of shape memory alloy actuator using resistance feedback control and its development". In: *Progress in Natural Science: Materials International* (2010). URL: `http://www.sciencedirect.com/science/article/pii/S1002007112600136`.

[58] Y. Teh and R. Featherstone. "A new control system for fast motion control of SMA actuator wires". In: (2004).

[59] H. Song, E. Kubica, and R. Gorbet. "Resistance modelling of SMA wire actuators". In: (2011). URL: https://www.ndt.net/article/ndtcanada2011/papers/66_Gorbet_Rev2.pdf.

[60] V. Novák, P. Šittner, G.N. Dayananda, F.M. Braz-Fernandes, and K.K. Mahesh. "Electric resistance variation of NiTi shape memory alloy wires in thermomechanical tests: Experiments and simulation". In: (2008). URL: http://www.sciencedirect.com/science/article/pii/S0921509307012117.

[61] R. Yousefian, M.A. Kia, and M.H. Zadeh. "Sensorless resistive-based control of shape memory alloy actuators in locking mechanism". In: *Journal of Intelligent Material Systems and Structures* (2015).

[62] URL: https://www.fwmetals.com/.

[63] Accessed: 2019-06-19. URL: https://no.rs-online.com/web/p/thermistor-ics/7691892/.

[64] Accessed: 2019-06-19. URL: www.https://no.rs-online.com/web/.

[65] Accessed: 2019-07-11. URL: https://us.flukecal.com/products/data-acquisition-and-test-equipment/data-acquisition/1586a-super-daq-precision-temperature-.

[66] Accessed: 2019-07-11. URL: https://us.flukecal.com/products/process-calibration-tools/temperature-calibrators/field-temperature-sources/9100s-9102s-han.

[67] Accessed: 2019-06-19. URL: https://www.tdk-electronics.tdk.com/inf/50/db/ntc_09/Glass_enc_Sensors__B57540__G540__G1540.pdf.

[68] Accessed: 2019-06-19. URL: https://no.rs-online.com/web/p/rotary-encoders/7899359/.

[69] Accessed: 2019-06-19. URL: https://docs-emea.rs-online.com/webdocs/12af/0900766b812af442.pdf.

[70] Accessed: 2019-06. URL: www.nordicneurolab.com/en/component/content/article/30-news/78-visualsystem?Itemid=101.

[71] Accessed: 2019-08-05. URL: https://www.toellner.de/datenblaetter/en_8732_8735.pdf.

[72] Accessed: 2019-08-05. URL: https://www.manualslib.com/manual/1218338/Ea-Elektro-Automatik-Ps-2042-06b.html.

[73] Accessed: 2019-08-05. URL: https://www.clasohlson.com/uk/Cocraft-Vernier-Caliper/40-8747.

[74] Accessed: 2019-08-05.

[75] John P. Bentley. *Principles of measurement systems*. Pearson Prentice Hall, 2006.

[76] Accessed: 2019-10-10. URL: https://www.analog.com/media/en/technical-documentation/data-sheets/AD8203.pdf.

[77] Accessed: 2019-09-25. URL: https://www.siemens-healthineers.com/magnetic-resonance-imaging/3t-mri-scanner/magnetom-prisma.

[78] Accessed: 2019-10-25. URL: https://www.siemens-healthineers.com/medical-imaging-it/advanced-visualization-solutions/syngo-fastview.

[79] Accessed: 2019-10-17. URL: https://upload.wikimedia.org/wikipedia/commons/e/e1/Human_anatomy_planes.svg.

[80] Accessed: 2019-10-17. URL: http://www.rfcafe.com/references/electrical/frequency-wavelength-conversion-table.htm.

[81] Accessed: 2019-10-17. URL: https://circuitglobe.com/kelvin-bridge.html.